Available online at www.sciencedirect.com
SCIENCE DIRECT®
Journal of Computational Physics 198 (2004) 686–726
JOURNAL OF COMPUTATIONAL PHYSICS
www.elsevier.com/locate/jcp

Wave overtopping over a sea dike

Tingqiu Li *, Peter Troch, Julien De Rouck

Department of Civil Engineering, Ghent University, Technologiepark 904, B-9052 Zwijnaarde, Belgium

Received 5 June 2003; received in revised form 15 January 2004; accepted 28 January 2004
Available online 27 February 2004

Abstract

This paper describes a solver on the simulation of overtopping of water waves over sloping and vertical structures in a numerical wave tank (NWT). It involves a time-implicit cell-staggered approximately factored VOF finite volume (FV) approach for solution of unsteady incompressible Navier–Stokes (NS) equations with a free surface on non-uniform Cartesian cut-cell grids. The Godunov-type high-order upwind schemes are introduced for discretization of the convective fluxes, while the coupling of the pressure with the velocity is realized by a projection method. The effects of turbulence are incorporated with a subgrid-scale (SGS) model. A novel VOF solver is proposed for the capture of a free surface undergoing severe topological deformation related with breaking waves. Only an approximation for the free-surface boundary conditions neglects the viscous stress but surface tension is modelled as a body force. A blend of second- and fourth-order artificial damping terms is designed for enhancement of the numerical stability. Additionally, the cut-cell techniques are utilized for handling an arbitrary geometry, and an absorbing-generating boundary condition for a wave generator is applied. The calculated results are represented in terms of the surface elevation versus time at certain locations and the velocity fields created by regular and irregular waves. Furthermore, the convergence behavior, the grid refinement effects, the study of different SGS models, the surface tension and Reynolds number effects and the role of a turbulence model under breaking waves are discussed, including a comparison with measurements available.

Keywords: The NS equations with a free-surface; Overtopping of breaking waves; A VOF-based finite volume solver; Nonuniform Cartesian cut-cell meshes

1. Introduction

Overtopping of waves over a sea dike is a violently natural phenomenon that may cause the structural failure of the sea defence. Owing to the presence of breaking waves, flows become highly turbulent, often subjected to rapid deformation of the free-surface. Of particular interest is the capture of breaking waves in the surf zone and elsewhere, which needs an investigation of the behavior of the moving air–water interface referred to as the free surface. A study on overtopping of waves in complex flows with high turbulence is

* Corresponding author. Tel.: +32-9-264-54-89; fax: +32-9-264-58-37.
E-mail address: tingqiu.li@UGent.be (T. Li).

0021-9991/$ - see front matter
doi:10.1016/j.jcp.2004.01.022

one of the challenging topics. An elucidation of the more detailed mechanism is essential and always desirable in research and engineering.

Theoretically, the relevant study involves the solution of moving boundary problems, where the effects of the free surface are distributed over a region proportional to several grids. Only its initial location and geometry are known a priori but the final location has to be determined as part of the solution. Consequently, the gross topology change undergoing the processes of merging and breakup amplifies wave-structure coupling problems. In particular, it tends to be more difficult in the presence of surface tension, including the treatment of the viscous dynamic free-surface boundary conditions [26], while the free surface is assigned as one of the boundaries in the computational domain. A powerful numerical tool, therefore, is preferred for handling the arbitrarily shaped interfaces naturally. Many approaches are available for studying flows of immiscible fluids with interfaces (see, for example, the density function method [38], a front-tracking approach [55], the smoothed particle hydrodynamics (SPH) [35], the level set method [37,49] and VOF plus their coupled approach [51]). Comprehensive reviews on breaking waves in the surf zone can be found in Christensen [6], Watanabe and Saeki [59] and Lin [32], based on a large-eddy simulation (LES) and the Reynolds-averaged Navier–Stokes (RANS) approximation, respectively. The volume-of-fluid (VOF) method is one of the most popular schemes so far. Its intrinsic feature is to identify the mass conservation, especially without special attention for modelling of topological changes of the front. On a stationary grid, one tracks the volume of each material in cells that contain a portion of an interface (defined as mixed cells), as long as the data α are specified according to the shape and location of an initial interface, where the volume fractions (denoted as α hereafter) satisfy $0 < \alpha < 1$, in which the value of $\alpha = \frac{1}{2}$ is supposed to represent the interfaces. It is shown that an iterative course of α includes a two-stage process: one is referred to as an interface reconstruction algorithm and one an advection algorithm for α.

1.1. An interface reconstruction algorithm

Typically, it is classified in two basic categories: an explicit/implicit interface reconstruction. For the former, the current many approaches [42] are to design an approximate interface (i.e., an Eulerian representation), dependent on the distributions of α at each time, called the modern PLIC (piecewise linear interface calculation) methods. By predefining various possible orientations, those can provide more exact approximation to the interfaces [40,61]. Alternative is to move the PLIC-type interfaces, for example, by virtue of a local velocity at a certain cell face, called Lagrangian interface reconstruction methods in the Lagrangian sense. In this way, the stretching or compression of the interface can be taken into account naturally during each single fractional step [14], consequently, it is thought as a more robust approach. For the latter, one assigns a piecewise-constant representation of the interface (e.g., the original Hirt and Nichols's VOF method [17]), named a purely Eulerian representation. Its significant advantage is that the interfaces arbitrarily orientated with respect to the computational grids are allowed.

1.2. An advection algorithm for α

One has to resolve the following transport equation:

$$\frac{\partial \alpha}{\partial t} + \frac{\partial (u\alpha)}{\partial x} + \frac{\partial (v\alpha)}{\partial y} + \frac{\partial (w\alpha)}{\partial z} = 0 \tag{1}$$

provided that the underlying velocity fields and the reconstructed interface are given simultaneously. Actually, α is a scalar quantity carrying the material information, therefore, Eq. (1) updates α over mixed cells but maintains $\alpha = 1$ or 0 in the water or air, respectively. Given an explicit interface reconstruction, it is relatively straightforward in its implementation for the evaluation of the convective fluxes of α, due to the geometrical information available. Such approaches, without diffusion of the front, are more promising

than the original VOF method but at the cost of algorithmic complexity [42], especially in three-dimensional (3D) situations, where the operations to be performed could be more complicated in the context of mergers and breakups, as compared with purely Eulerian methods [54]. With the interfaces reconstructed implicitly, the critical issue is to treat the convective terms but this faces fundamental difficulties when the hyperbolic nonlinear partial differential equation of α (see Eq. (1)) is discretized on a finite grid. The use of regular high-resolution schemes, for example, leads to more or less diffusive on the evolution of α so that non-physical shape of the interface occurs over a few cells when the excessive diffusion is generated [15,24,46]. A similar phenomenon holds for the original VOF method, that is, a very popular one, because of its simplicity. Some reasons may be interpreted as the fact that it does not preserve local boundedness. To suppress such problem, a high resolution method with bounding treatments, called as CICSM [53] (compressive interface capturing scheme for arbitrary meshes), is proposed. The relevant study can be found in Rudman [46] and Xiao [60], respectively.

In this paper, we develop a new solver for modelling of overtopping of waves over vertical and sloping coastal structures. Applications to the capture of breaking waves are emphasized in our solver for illustration of its particular feature to case studies related to wave overtopping. This solver includes an operator-split implicit-time differencing scheme for resolution of the NS equations on nonuniform Cartesian cut-cell meshes with the help of a cell-staggered finite volume (FV) method, while incompressibility is realized by enforcing an iterative Poisson solver for the pressure. A sharp interface in topologically complex wave-induced flows is tracked with the VOF-based algorithm easy to use but to well describe the physical behavior of practical problems. All that is necessary involves the need for eliminating the knowledge of detailed interface information at each iteration plus an implicit treatment for the surface pressure. In the latter case, this considers the contribution from the air, only applying the pressure on the water. Additionally, surface tension is enforced as a body force according to the continuum surface force (CSF) model [4]. This allows to significantly simplify the normal dynamic free-surface boundary condition. In our study, the pressure at mixed cells is incorporated into the corresponding field equation. In particular, no explicit expression for the interface reconstruction is required during tracking, which is similar to the level set method widely applied to many fields. As expected, it can be generalized well to 3D and used for several industrial applications as well. Our work in this area is to develop an approach that preserves the smoothness of the interface and maintains its sharp definition over one cell, indicating that numerical diffusion related with upwind schemes should not be excessive (that is, without dispersing or wrinkling). It is composed of a weighted upwind scheme with the help of an operator-split second-order explicit Adams–Bashforth advection algorithm plus a blending scheme. For two test cases that involve complex wave-induced flows, our computation demonstrates that the approach proposed is simple and computationally efficient.

This paper is organized as follows. First, we outline the numerical methods that include the mathematical model, a fully implicit cell-staggered FV approach on nonuniform Cartesian cut-cell grids, the modelling of surface tension, a novel solution for the volume fractions α and a static Smagorinsky model with a constant coefficient, respectively. The calculated results and discussions, such as some convergence properties, the study of grid refinement effects, the investigation of two different SGS models, the Reynolds number and surface tension effects, and the wave-induced flows plus comparison with the experimental date available, are represented next, followed by the concluding remarks.

2. Methodology

2.1. Mathematical model

For sea dike problems, a right-handed coordinate system (x, y, z) is set up, as illustrated in Fig. 1, where the origin is fixed at the intersection of the inlet with the still water level (SWL), and three coordinates

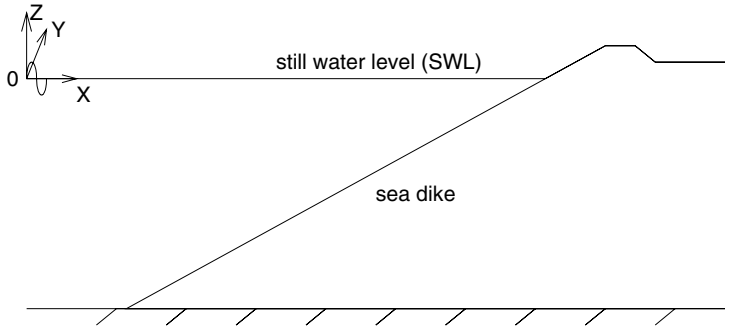

Fig. 1. A reference coordinate system for sea dike problems.

(x, y, z) are defined as positive in the direction of the wave propagation, towards the width of a dike and upwards, respectively. Assuming that the mathematical model is based on unsteady incompressible Navier–Stokes (NS) equations in a conservative form on Cartesian grids, thus one has

$$\frac{\partial \varphi}{\partial t} + \frac{\partial F}{\partial x} + \frac{\partial G}{\partial y} + \frac{\partial H}{\partial z} = Q, \tag{2}$$

where variables $\varphi = (0, u, v, w)^{\mathrm{T}}$. $(F, G, H) = (F_{\mathrm{i}} - F_{\mathrm{v}} + F_{\mathrm{a}}, G_{\mathrm{i}} - G_{\mathrm{v}} + G_{\mathrm{a}}, H_{\mathrm{i}} - H_{\mathrm{v}} + H_{\mathrm{a}})$ are expressed as, respectively,

$$F_{\mathrm{i}} = \begin{pmatrix} 0 \\ u^2 \\ vu \\ wu \end{pmatrix}, \quad G_{\mathrm{i}} = \begin{pmatrix} 0 \\ uv \\ v^2 \\ wv \end{pmatrix}, \quad H_{\mathrm{i}} = \begin{pmatrix} 0 \\ uw \\ vw \\ w^2 \end{pmatrix} \tag{3}$$

for the inviscid fluxes $(F_{\mathrm{i}}, G_{\mathrm{i}}, H_{\mathrm{i}})$,

$$F_{\mathrm{v}} = \begin{pmatrix} 0 \\ \nu_{\mathrm{eff}} \frac{\partial u}{\partial x} \\ \nu_{\mathrm{eff}} \frac{\partial v}{\partial x} \\ \nu_{\mathrm{eff}} \frac{\partial w}{\partial x} \end{pmatrix}, \quad G_{\mathrm{v}} = \begin{pmatrix} 0 \\ \nu_{\mathrm{eff}} \frac{\partial u}{\partial y} \\ \nu_{\mathrm{eff}} \frac{\partial v}{\partial y} \\ \nu_{\mathrm{eff}} \frac{\partial w}{\partial y} \end{pmatrix}, \quad H_{\mathrm{v}} = \begin{pmatrix} 0 \\ \nu_{\mathrm{eff}} \frac{\partial u}{\partial z} \\ \nu_{\mathrm{eff}} \frac{\partial v}{\partial z} \\ \nu_{\mathrm{eff}} \frac{\partial w}{\partial z} \end{pmatrix} \tag{4}$$

for the viscous fluxes $(F_{\mathrm{v}}, G_{\mathrm{v}}, H_{\mathrm{v}})$,

$$F_{\mathrm{a}} = \begin{pmatrix} u \\ \frac{1}{\rho} p \\ 0 \\ 0 \end{pmatrix}, \quad G_{\mathrm{a}} = \begin{pmatrix} v \\ 0 \\ \frac{1}{\rho} p \\ 0 \end{pmatrix}, \quad H_{\mathrm{a}} = \begin{pmatrix} w \\ 0 \\ 0 \\ \frac{1}{\rho} p \end{pmatrix} \tag{5}$$

for the acoustic fluxes $(F_{\mathrm{a}}, G_{\mathrm{a}}, H_{\mathrm{a}})$, and

$$Q = \begin{pmatrix} 0 \\ \frac{1}{\rho} F_{\mathrm{b}}^{x} \\ \frac{1}{\rho} F_{\mathrm{b}}^{y} \\ \frac{1}{\rho} F_{\mathrm{b}}^{z} - g \end{pmatrix} \tag{6}$$

for the source term (Q). (u, v, w) are the components of the velocity in the x-, y- and z-directions, respectively, p is the total pressure, and g is the gravitational acceleration. (F_b^x, F_b^y, F_b^z) are three components of a body force $\vec{F}_b$ in the (x, y, z)-directions, respectively. v_{eff} is the effective viscous coefficient by setting $v_{eff} = v + v_t$, in which v is the molecular kinematic viscosity and the eddy viscosity v_t has to be determined with a turbulence model. The local density ρ and viscosity v_{eff} are given as in terms of α

$$\rho = \alpha\rho_w + (1-\alpha)\rho_a, \quad v_{eff} = \alpha v_{eff_w} + (1-\alpha)v_{eff_a}, \tag{7}$$

where the subscripts (w, a) denote the water and the air, respectively.

2.2. A fully implicit cell-staggered finite volume method

With a staggered grid arrangement, the pressure is coupled with the velocity naturally. The benefit is that its use helps to avoid some types of convergence problems and oscillations in the pressure and velocity fields [9]. In this way, the pressure and α are located at the centre of a cell, while three components (u, v, w) of the velocity lie in the centre of the $(i+\frac{1}{2})$, $(j+\frac{1}{2})$ and $(k+\frac{1}{2})$ faces enclosed a cell (ijk), respectively (see Fig. 2). With an implicit FV method, the discretization of the integral form of Eq. (2) over each cell may be written by

$$\left(\frac{\partial\varphi}{\partial t}\right)^{n+1} + \frac{1}{V}\sum_{\text{faces}} \overline{F}^{n+1} = Q^{n+1} \tag{8}$$

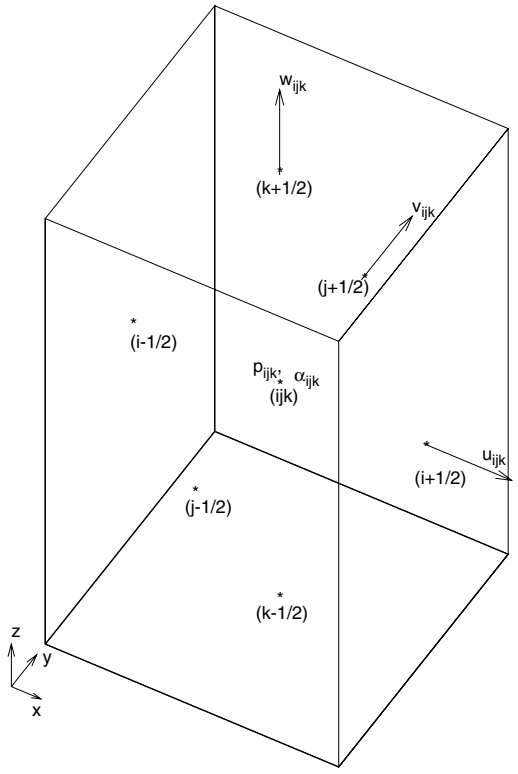

Fig. 2. A staggered grid system. (p_{ijk}, α_{ijk}) are defined at the center of a cell (i, j, k); $(u_{ijk}, v_{ijk}, w_{ijk})$ at the faces $(i+1/2, j, k)$, $(i, j+1/2, k)$ and $(i, j, k+1/2)$, respectively.

for an arbitrary fixed volume V with a cell face S. The subscript faces represents the summation over all cell faces surrounding a hexahedral cell. $\overline{F} = (Fn_x + Gn_y + Hn_z)S$, where (n_x, n_y, n_z) are the unit normal components of the cell face outwards in the x-, y- and z-directions, respectively.

Since there is no restriction of time step level, in principle, an implicit approach provides a more efficient way in studying slowly transient flows. Nevertheless, it is not realistic to resolve a large coupled set of non-linear equations at each time step. Consequently, various approaches are proposed for an approximation of Eq. (8). In this study, the variation of the unknown fluxes at the $(n+1)$th time step is obtained with the introduction of the so-called Delta form [25,34,44], indicating that a local linearization of the fluxes created by the convective and diffusion terms, respectively, is enforced. As a result, the fluxes at the $(n+1)$th time step is formulated by a Taylor series extension to first-order accuracy in terms of the time t. Namely

$$\overline{F}^{n+1} = \overline{F}^n + \frac{\partial \overline{F}}{\partial t}\Delta t = \overline{F}^n + \frac{\partial \overline{F}}{\partial \varphi}\frac{\partial \varphi}{\partial t}\Delta t = \overline{F}^n + \frac{\partial \overline{F}}{\partial \varphi}\delta\varphi,$$

where the Delta form $\delta\varphi = \varphi^{n+1} - \varphi^n$. Hence, one has

$$\delta\varphi + \frac{\Delta t}{V}\sum_{\text{faces}}\left(\frac{\partial \overline{F}}{\partial \varphi}\right)\delta\varphi = \Delta t R.$$

By setting $\overline{F} = \overline{F}_{\text{i}} - \overline{F}_{\text{v}}$, it can be derived by

$$\begin{aligned}
&\delta\varphi + \frac{\Delta t}{V}\left\{\left[\left(\frac{\partial \overline{F}_{\text{i}}}{\partial \varphi} - \frac{\partial \overline{F}_{\text{v}}}{\partial \varphi}\right)\delta\varphi\right]_{i+\frac{1}{2}} - \left[\left(\frac{\partial \overline{F}_{\text{i}}}{\partial \varphi} - \frac{\partial \overline{F}_{\text{v}}}{\partial \varphi}\right)\delta\varphi\right]_{i-\frac{1}{2}}\right\} + \frac{\Delta t}{V}\left\{\left[\left(\frac{\partial \overline{F}_{\text{i}}}{\partial \varphi} - \frac{\partial \overline{F}_{\text{v}}}{\partial \varphi}\right)\delta\varphi\right]_{j+\frac{1}{2}}\right.\\
&\quad\left. - \left[\left(\frac{\partial \overline{F}_{\text{i}}}{\partial \varphi} - \frac{\partial \overline{F}_{\text{v}}}{\partial \varphi}\right)\delta\varphi\right]_{j-\frac{1}{2}}\right\} + \frac{\Delta t}{V}\left\{\left[\left(\frac{\partial \overline{F}_{\text{i}}}{\partial \varphi} - \frac{\partial \overline{F}_{\text{v}}}{\partial \varphi}\right)\delta\varphi\right]_{k+\frac{1}{2}} - \left[\left(\frac{\partial \overline{F}_{\text{i}}}{\partial \varphi} - \frac{\partial \overline{F}_{\text{v}}}{\partial \varphi}\right)\delta\varphi\right]_{k-\frac{1}{2}}\right\}\\
&\quad = \Delta t R
\end{aligned} \tag{9}$$

with the residual of the momentum equations R defined as

$$R = -\left\{\frac{1}{V}\sum_{\text{faces}}\overline{F}^n - Q^n\right\} = -\left\{\frac{1}{V}\sum_{\text{faces}}\left(\overline{F}_{\text{i}}^n - \overline{F}_{\text{v}}^n\right) - Q^n\right\}, \tag{10}$$

where $\overline{F}_{\text{i}} = F_{\text{i}}n_x + G_{\text{i}}n_y + H_{\text{i}}n_z$ and $\overline{F}_{\text{v}} = F_{\text{v}}n_x + G_{\text{v}}n_y + H_{\text{v}}n_z$. Clearly, $\overline{F}_{\text{i}}$ and $\overline{F}_{\text{v}}$ represent the contributions from the inviscid and viscid fluxes in the (x, y, z)-directions, respectively. This implies that the body force $\vec{F}_{\text{b}}$ and the acoustic fluxes are not involved in the currently implicit process, except for the source terms, $Q^{n+1} = Q^n = (0, 0, 0, -g)^{\text{T}}$. In this case, the summation is taken over six cell faces surrounding a cell (ijk) via $\sum_{\text{faces}} = (\,)_{i+\frac{1}{2}} - (\,)_{i-\frac{1}{2}} + (\,)_{j+\frac{1}{2}} - (\,)_{j-\frac{1}{2}} + (\,)_{k+\frac{1}{2}} - (\,)_{k-\frac{1}{2}}$, as shown in Fig. 2.

2.2.1. Evaluation of the derivatives $\frac{\partial \overline{F}_{\text{i}}}{\partial \varphi}$ and $\frac{\partial \overline{F}_{\text{v}}}{\partial \varphi}$ at a certain face

In our implicit stage, the derivative $\frac{\partial \overline{F}}{\partial \varphi}$ is decomposed as two terms $\frac{\partial \overline{F}_{\text{i}}}{\partial \varphi}$ and $\frac{\partial \overline{F}_{\text{v}}}{\partial \varphi}$, respectively. For the evaluation of the corresponding values, we adopt the two different approximations: one [25,44] is to use an one-order upwind scheme for achievement of $\frac{\partial \overline{F}_{\text{i}}}{\partial \varphi}$; one [25,34] is to neglect the cross derivatives related with the viscid fluxes, when calculating $\frac{\partial \overline{F}_{\text{v}}}{\partial \varphi}$ with a central-difference scheme. The former maintains the bandwidth of tridiagonal block in the linear equation, resulting in lower memory for the solution of Eq. (9); the latter allows to significantly simplify the expression in the matrix.

2.2.1.1. Computation of $\frac{\partial \overline{F}_i}{\partial \varphi}$. The convective fluxes in the x-momentum equation, for example, may be derived by

$$\frac{\partial uu}{\partial x}+\frac{\partial vu}{\partial y}+\frac{\partial wu}{\partial z}=\frac{1}{V}\sum_{\text{faces}}u_n uS=\frac{1}{V}\sum_{\text{faces}}\dot{M}u=\frac{1}{V}\sum_{\text{faces}}\overline{F}_i, \tag{11}$$

where the normal face velocity u_n is defined as

$$u_n=un_x+vn_y+wn_z \tag{12}$$

so that the inviscid volumetric $\dot{M}$ and momentum fluxes $\overline{F}_i$ across a certain face are, respectively,

$$\dot{M}=u_nS \quad \text{and} \quad \overline{F}_i=\dot{M}u.$$

The latter results in the derivative $\frac{\partial \overline{F}_i}{\partial u}$, such as at the $(i+\frac{1}{2})$ face, as

$$\left(\frac{\partial \overline{F}_i}{\partial u}\right)_{i+\frac{1}{2}}=\dot{M}_{i+\frac{1}{2}}$$

on the assumption that $\dot{M}_{i+\frac{1}{2}}$ is unchanged at one currently iterative cycle. With an one-order upwind scheme, therefore,

$$\left(\frac{\partial \overline{F}_i}{\partial \varphi}\delta\varphi\right)_{i+\frac{1}{2}}$$

can be given as

$$\left(\frac{\partial \overline{F}_i}{\partial \varphi}\delta\varphi\right)_{i+\frac{1}{2}}=\left(\dot{M}\delta\varphi\right)_{i+\frac{1}{2}}=\dot{M}^+_{i+\frac{1}{2}}\delta\varphi_i-\dot{M}^-_{i+\frac{1}{2}}\delta\varphi_{i+1} \tag{13}$$

in which $\dot{M}^+_{i+\frac{1}{2}}$ and $\dot{M}^-_{i+\frac{1}{2}}$ are formulated by, respectively,

$$\dot{M}^+_{i+\frac{1}{2}}=\max\left(\dot{M}_{i+\frac{1}{2}},0\right), \quad \dot{M}^-_{i+\frac{1}{2}}=\max\left(-\dot{M}_{i+\frac{1}{2}},0\right).$$

The subscripts $(i,i+1)$ represent cells, respectively, as shown in Fig. 3. Owing to $\max(x,0)=\max(-x,0)+x$, for example, $\dot{M}^+_{i+\frac{1}{2}}$ can be split as $\dot{M}^+_{i+\frac{1}{2}}=\dot{M}_{i+\frac{1}{2}}+\dot{M}^-_{i+\frac{1}{2}}$, which is useful when one arranges Eq. (17).

2.2.1.2. Evaluation of $\frac{\partial \overline{F}_v}{\partial \varphi}$. For the viscous fluxes in the x-momentum equation (i.e., $\varphi=u$), it reads as

$$v_{\text{eff}}\left(\frac{\partial^2\varphi}{\partial x^2}+\frac{\partial^2\varphi}{\partial y^2}+\frac{\partial^2\varphi}{\partial z^2}\right)=\frac{v_{\text{eff}}}{V}\sum_{\text{faces}}\frac{\partial\varphi}{\partial n}S=\frac{1}{V}\sum_{\text{faces}}\overline{F}_v, \tag{14}$$

where $\frac{\partial\varphi}{\partial n}$ is the normal gradient at a certain face defined by

$$\frac{\partial\varphi}{\partial n}=\frac{\partial\varphi}{\partial x}n_x+\frac{\partial\varphi}{\partial y}n_y+\frac{\partial\varphi}{\partial z}n_z$$

so that the viscous momentum flux $\overline{F}_v$ is

$$\overline{F}_v=v_{\text{eff}}\frac{\partial\varphi}{\partial n}S. \tag{15}$$

With a central difference scheme,

$$\left(\frac{\partial \overline{F}_v}{\partial \varphi}\delta\varphi\right)_{i+\frac{1}{2}},$$

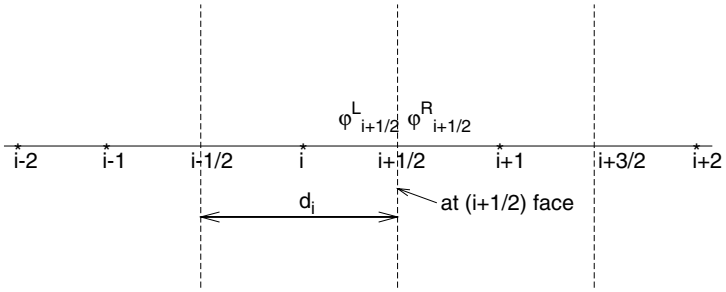

Fig. 3. Denotation of the variable values of the left ($\varphi^{\mathrm{L}}_{i+\frac{1}{2}}$) and right ($\varphi^{\mathrm{R}}_{i+\frac{1}{2}}$) states at the $(i+\frac{1}{2})$ face over a cell (i). $(i-2, i-1, i+1, i+2)$ represent the corresponding cells, respectively.

such as at the $(i+\frac{1}{2})$ face, can be written as

$$\left(\frac{\partial \overline{F}_{\mathrm{v}}}{\partial \varphi}\delta\varphi\right)_{i+\frac{1}{2}} = v_{\mathrm{eff}}\frac{\partial}{\partial \varphi}\left(\frac{\partial \varphi}{\partial n}S\right)_{i+\frac{1}{2}}\delta\varphi = \left(\delta\varphi_{i+1}-\delta\varphi_i\right)K_{i+\frac{1}{2}}, \tag{16}$$

where $K_{i+\frac{1}{2}} = (\frac{v_{\mathrm{eff}}S}{\Delta x})_{i+\frac{1}{2}}$ is the viscous volumetric fluxes, in which Δx is the corresponding cell thickness (see Fig. 4). In this way, the bandwidth of the linear equation is kept as a set of tridiagonal block that may be resolved by the alternative directional implicit (ADI) approach.

2.2.2. Solution of the Delta form $\delta\varphi$

Owing to $\overline{F} = \overline{F}_{\mathrm{i}} - \overline{F}_{\mathrm{v}}$, $A_{(i\pm1)}$ may be defined as a blend of two nondimensional coefficients associated with the inviscid volumetric fluxes $(\dot{M})$ and the viscous fluxes (K), respectively,

$$A_{i+1} = \frac{\Delta t}{V}\left(K_{i+\frac{1}{2}} + \dot{M}^{-}_{i+\frac{1}{2}}\right), A_{i-1} = \frac{\Delta t}{V}\left(K_{i-\frac{1}{2}} + \dot{M}^{+}_{i-\frac{1}{2}}\right).$$

Substituting Eqs. (13) and (16) into Eq. (9), it can be factored into the following three one-dimensional equations:

$$\begin{aligned}
&-A_{i-1}\delta\varphi^{**}_{i-1} + A^{(1)}_p\delta\varphi^{**} - A_{i+1}\delta\varphi^{**}_{i+1} = \Delta t R,\\
&-A_{j-1}\delta\varphi^{*}_{j-1} + A^{(2)}_p\delta\varphi^{*} - A_{j+1}\delta\varphi^{*}_{j+1} = \delta\varphi^{**},\\
&-A_{k-1}\delta\varphi_{k-1} + A^{(3)}_p\delta\varphi - A_{k+1}\delta\varphi_{k+1} = \delta\varphi^{*},
\end{aligned} \tag{17}$$

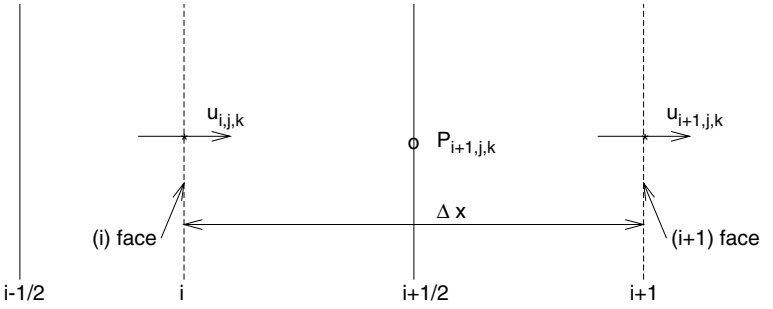

Fig. 4. A shifted control volume surrounding $P_{i+1,j,k}$ for discretization of the gradient $\frac{\partial u}{\partial n}$ at the face $(i+\frac{1}{2})$. $(i, i+1)$ represent its cell face in the principal direction, respectively.

according to the ADI algorithm. The mainly diagonal coefficients $A_p^{(1)}, A_p^{(2)}$ and $A_p^{(3)}$ in Eq. (17) are expressed as, respectively,

$$A_p^{(1)} = 1 + A_{i+1} + A_{i-1} + \frac{\Delta t}{V}\left(\dot{M}_{i+\frac{1}{2}} - \dot{M}_{i-\frac{1}{2}}\right),$$
$$A_p^{(2)} = 1 + A_{j+1} + A_{j-1} + \frac{\Delta t}{V}\left(\dot{M}_{j+\frac{1}{2}} - \dot{M}_{j-\frac{1}{2}}\right),$$
$$A_p^{(3)} = 1 + A_{k+1} + A_{k-1} + \frac{\Delta t}{V}\left(\dot{M}_{k+\frac{1}{2}} - \dot{M}_{k-\frac{1}{2}}\right),$$

where (i, j, k) denote the cell number in the x-, y- and z-directions, respectively. $(i+1)$ and $(i-1)$ are two neighbours of cell i (see Fig. 3). Similar definition is for $A_{j\pm1}$ and $A_{k\pm1}$ by index substitution. For achievement of $\delta\varphi$, one requires to resolve the tridiagonal systems (see Eq. (17)), which may be accomplished with ease based on TDMA (tridiagonal matrix algorithm).

2.2.3. Evaluation of the temporal velocity $\tilde{\varphi}$

The following temporal velocity $\tilde{\varphi}$ is renewed

$$\tilde{\varphi} = \varphi^n + \delta\varphi + \frac{1}{\rho}F_{\mathrm{b}}^i \tag{18}$$

provided that $\delta\varphi$ is available from Eq. (17). The last term $\frac{1}{\rho}F_{\mathrm{b}}^i$ in Eq. (18) is to account for the contribution of surface tension. It may be simulated with the help of the CSF model. $(F_{\mathrm{b}}^1, F_{\mathrm{b}}^2, F_{\mathrm{b}}^3) = (F_{\mathrm{b}}^x, F_{\mathrm{b}}^y, F_{\mathrm{b}}^z),\ i = 1, 2, 3.$

2.2.4. A Poisson equation for the pressure

The temporal velocity $\tilde{\varphi} = (\tilde{u}, \tilde{v}, \tilde{w})$ is not, in general, divergence-free but always used to update the pressure according to the projected algorithm [7]. Consequently, the final velocity field is enforced to satisfy the continuity equation: $\nabla \cdot \vec{u} = 0$. Accordingly, substituting the resulting velocity (i.e., with a backward Euler method)

$$\begin{aligned} u^{n+1} &= \tilde{u} - \frac{\Delta t}{\rho}\frac{\partial p^{n+1}}{\partial x}, \\ v^{n+1} &= \tilde{v} - \frac{\Delta t}{\rho}\frac{\partial p^{n+1}}{\partial y}, \\ w^{n+1} &= \tilde{w} - \frac{\Delta t}{\rho}\frac{\partial p^{n+1}}{\partial z} \end{aligned} \tag{19}$$

into the following continuity equation,

$$\sum_{\text{faces}} \left\{\left(u^{n+1}n_x + v^{n+1}n_y + w^{n+1}n_z\right)S\right\} = 0 \tag{20}$$

this yields

$$\sum_{\text{faces}} \left\{\frac{1}{\rho}\left(\frac{\partial p^{n+1}}{\partial x}n_x + \frac{\partial p^{n+1}}{\partial y}n_y + \frac{\partial p^{n+1}}{\partial z}n_z\right)S\right\} = \frac{1}{\Delta t}\sum_{\text{faces}}\left\{\left(\tilde{u}n_x + \tilde{v}n_y + \tilde{w}n_z\right)S\right\}.$$

Furthermore, it may be rewritten as

$$\begin{aligned}
&\left\{\frac{1}{\rho}\left(\frac{\partial p^{n+1}}{\partial n}\right)S\right\}_{i+\frac{1}{2}} - \left\{\frac{1}{\rho}\left(\frac{\partial p^{n+1}}{\partial n}\right)S\right\}_{i-\frac{1}{2}} \\
&\left\{\frac{1}{\rho}\left(\frac{\partial p^{n+1}}{\partial n}\right)S\right\}_{j+\frac{1}{2}} - \left\{\frac{1}{\rho}\left(\frac{\partial p^{n+1}}{\partial n}\right)S\right\}_{j-\frac{1}{2}} \\
&\left\{\frac{1}{\rho}\left(\frac{\partial p^{n+1}}{\partial n}\right)S\right\}_{k+\frac{1}{2}} - \left\{\frac{1}{\rho}\left(\frac{\partial p^{n+1}}{\partial n}\right)S\right\}_{k-\frac{1}{2}} = \widehat{R}
\end{aligned} \tag{21}$$

with the following source term $\widehat{R}$

$$\widehat{R} = \frac{1}{\Delta t}\left\{(\widehat{u}_n S)_{i+\frac{1}{2}} - (\widehat{u}_n S)_{i-\frac{1}{2}} + (\widehat{u}_n S)_{j+\frac{1}{2}} - (\widehat{u}_n S)_{j-\frac{1}{2}} + (\widehat{u}_n S)_{k+\frac{1}{2}} - (\widehat{u}_n S)_{k-\frac{1}{2}}\right\},$$

where $\widehat{u}_n = \tilde{u}n_x + \tilde{v}n_y + \tilde{w}n_z$ and $\frac{\partial p}{\partial n} = \frac{\partial p}{\partial x}n_x + \frac{\partial p}{\partial y}n_y + \frac{\partial p}{\partial z}n_z$ are the normal face velocity and the pressure gradient at a certain face, respectively.

Using a central-difference scheme, Eq. (21) is discretized with respect to the pressure gradients on the cell faces so that it can be cast into the following seven-point stencil form:

$$\begin{aligned}
&A_{i,j,k}p^{n+1}_{i,j,k} + B^{\mathrm{l}}_{i-1,j,k}p^{n+1}_{i-1,j,k} + B^{\mathrm{u}}_{i+1,j,k}p^{n+1}_{i+1,j,k} + C^{\mathrm{l}}_{i,j-1,k}p^{n+1}_{i,j-1,k} \\
&\quad + C^{\mathrm{u}}_{i,j+1,k}p^{n+1}_{i,j+1,k} + D^{\mathrm{l}}_{i,j,k-1}p^{n+1}_{i,j,k-1} + D^{\mathrm{u}}_{i,j,k+1}p^{n+1}_{i,j,k+1} = \widehat{R}.
\end{aligned} \tag{22}$$

Eq. (22) may be thought as a discrete version of the Poisson-type equation for the pressure. Its relevant coefficients are

$$\begin{aligned}
A_{i,j,k} &= -\left(\frac{A_1}{\rho_{i+\frac{1}{2}}} + \frac{A_3}{\rho_{i-\frac{1}{2}}} + \frac{B_1}{\rho_{j+\frac{1}{2}}} + \frac{B_3}{\rho_{j-\frac{1}{2}}} + \frac{C_1}{\rho_{k+\frac{1}{2}}} + \frac{C_3}{\rho_{k-\frac{1}{2}}}\right), \\
B^{\mathrm{l}}_{i-1,j,k} &= \frac{A_3}{\rho_{i-\frac{1}{2}}}, \quad B^{\mathrm{u}}_{i+1,j,k} = \frac{A_1}{\rho_{i+\frac{1}{2}}}, \quad C^{\mathrm{l}}_{i,j-1,k} = \frac{B_3}{\rho_{j-\frac{1}{2}}}, \\
C^{\mathrm{u}}_{i,j+1,k} &= \frac{B_1}{\rho_{j+\frac{1}{2}}}, \quad D^{\mathrm{l}}_{i,j,k-1} = \frac{C_3}{\rho_{k-\frac{1}{2}}}, \quad D^{\mathrm{u}}_{i,j,k+1} = \frac{C_1}{\rho_{k+\frac{1}{2}}},
\end{aligned}$$

where the multipliers (A_1 to C_3) are defined as $A_1 = S_{i+\frac{1}{2}}d_i^{-1}$, $A_3 = S_{i-\frac{1}{2}}d_{i-1}^{-1}$, $B_1 = S_{j+\frac{1}{2}}d_j^{-1}$, $B_3 = S_{j-\frac{1}{2}}d_{j-1}^{-1}$, $C_1 = S_{k+\frac{1}{2}}d_k^{-1}$ and $C_3 = S_{k-\frac{1}{2}}d_{k-1}^{-1}$, respectively. The subscripts, such as $(i-1, i, i+1)$ and d_i, are shown in Fig. 3. $(\rho_{i\pm\frac{1}{2}}, S_{i\pm\frac{1}{2}})$ represent the corresponding face density and area, respectively. For the former, it may be determined with a weighted approach, since ρ is located at the center of a cell. The superscripts (l,u) denote the lower and upper diagonals, respectively.

On Cartesian grids, the discrete approximation to the derivatives forms a seven-point stencil in the linear system diagonally dominant. Owing to be positive definite and sparsity, it may be resolved by the iterative solution methods like the ICCG (incomplete Cholesky conjugate gradient) algorithm [22] or the SOR (successive over-relaxation) scheme.

Based on a quadratic backward approximation in time, an implicit three-level second-order scheme is implemented for the time derivative:

$$\left(\frac{\partial \varphi}{\partial t}\right)^{n+1} = \frac{3\varphi^{n+1} - 4\varphi^n + \varphi^{n-1}}{2\Delta t} = \frac{\frac{3}{2}\varphi^{n+1} - 2\varphi^n + \frac{1}{2}\varphi^{n-1}}{\Delta t},$$

where the superscripts $(n+1, n, n-1)$ stand for the next, current and previous time levels, respectively. Instead of Eq. (19), therefore, the resulting velocity at the $(n+1)$th time level is rewritten as (by setting $2\varphi^n \simeq \varphi^n + \tilde{\varphi}$)

$$\varphi^{n+1} = \frac{2}{3}\left(\varphi^n - \frac{1}{2}\varphi^{n-1} + \tilde{\varphi} - \frac{\Delta t}{\rho}\frac{\partial p}{\partial x_i}\right) \tag{23}$$

provided that the pressure from the Poisson solver is available. With the tensor notation, $x_i = (x_1, x_2, x_3) = (x, y, z), i = 1, 2, 3$. Owing to the strong coupling of the velocity with the pressure under waves breaking, one under-relaxation technique is implemented for the final velocity.

2.2.5. Evaluation of the explicit inviscid and viscid fluxes

2.2.5.1. Explicit inviscid fluxes $\overline{F}_{\mathrm{i}}^n$. At the nth time step, for example, the explicit inviscid fluxes, $\sum_{\text{faces}} \overline{F}_{\mathrm{i}}^n$ (see Eq. (10)) at the face $(i+\frac{1}{2})$, are evaluated by the flux-difference splitting approach [43]:

$$\left(\overline{F}_{\mathrm{i}}\right)_{i+\frac{1}{2}} = \frac{1}{2}\left\{\overline{F}_{\mathrm{i}}\left(\varphi^{\mathrm{R}}_{i+\frac{1}{2}}\right) + \overline{F}_{\mathrm{i}}\left(\varphi^{\mathrm{L}}_{i+\frac{1}{2}}\right)\right\} - \frac{1}{2}|A|\left(\varphi^{R}_{i+\frac{1}{2}} - \varphi^{L}_{i+\frac{1}{2}}\right) \tag{24}$$

with

$$\overline{F}_{\mathrm{i}}\left(\varphi^{\mathrm{R}}_{i+\frac{1}{2}}\right) = \left(\dot{M}\varphi^{\mathrm{R}}\right)_{i+\frac{1}{2}}, \quad \overline{F}_{\mathrm{i}}\left(\varphi^{\mathrm{L}}_{i+\frac{1}{2}}\right) = \left(\dot{M}\varphi^{\mathrm{L}}\right)_{i+\frac{1}{2}} \quad \text{and} \quad A = \left(\frac{\partial \overline{F}_{\mathrm{i}}}{\partial \varphi}\right)_{i+\frac{1}{2}}$$

indicating that the value of $\varphi_{i+\frac{1}{2}}$ at the face $(i+\frac{1}{2})$ is given by

$$\varphi_{i+\frac{1}{2}} = \begin{cases} \varphi^{\mathrm{R}}_{i+\frac{1}{2}} & \text{if } \dot{M}_{i+\frac{1}{2}} < 0; \\ \varphi^{\mathrm{L}}_{i+\frac{1}{2}} & \text{otherwise,} \end{cases}$$

where $\varphi^{\mathrm{L}}_{i+\frac{1}{2}}$ and $\varphi^{\mathrm{R}}_{i+\frac{1}{2}}$ are the variable values of the left and right states at the $(i+\frac{1}{2})$ face over one cell (i), respectively, as illustrated in Fig. 3. These may be obtained with the MUSCL (monotone upstream-centred scheme for conservation laws)-type TVD (total variation diminishing) scheme [56] or a second-order ENO (essential nonoscillation) scheme [49]. In the former case, $\varphi^{\mathrm{L}}_{i+\frac{1}{2}}$ and $\varphi^{\mathrm{R}}_{i+\frac{1}{2}}$ for one-dimensional problem are formulated by the k ($k = \frac{1}{3}$, a value we adopted) family of the MUSCL scheme:

$$\begin{aligned} \varphi^{L}_{i+\frac{1}{2}} &= \varphi_i + \frac{1}{4}(1-k)(\varphi_i - \varphi_{i-1}) + \frac{1}{4}(1+k)\left(\varphi_{i+1} - \varphi_i\right), \\ \varphi^{R}_{i+\frac{1}{2}} &= \varphi_{i+1} - \frac{1}{4}(1+k)\left(\varphi_{i+1} - \varphi_i\right) - \frac{1}{4}(1-k)\left(\varphi_{i+2} - \varphi_{i+1}\right). \end{aligned} \tag{25}$$

In the latter case, these are expressed as:

$$\begin{aligned} \varphi^{\mathrm{L}}_{i+\frac{1}{2}} &= \varphi_i + \frac{1}{2}m\left(\varphi_{i+1} - \varphi_i, \varphi_i - \varphi_{i-1}\right), \\ \varphi^{\mathrm{R}}_{i+\frac{1}{2}} &= \varphi_{i+1} - \frac{1}{2}m\left(\varphi_{i+2} - \varphi_{i+1}, \varphi_{i+1} - \varphi_i\right), \end{aligned} \tag{26}$$

where the subscripts $(i-1, i, i+1, i+2)$ used are shown in Fig. 3, and the function $m(a, b)$ is defined as

$$m(a, b) = \begin{cases} a & \text{if } |a| \leqslant |b|, \\ b & \text{otherwise.} \end{cases}$$

In the smooth regions, the MUSCL scheme and the ENO one approximate the convective flux differencing with a second-order accuracy. Instead of the two approaches, the following one-order upwind scheme is imposed in cells adjoining the interface and the wall:

$$\begin{aligned}\varphi^L_{i+\frac{1}{2}} &= \varphi_i,\\ \varphi^R_{i+\frac{1}{2}} &= \varphi_{i+1}.\end{aligned} \tag{27}$$

2.2.5.2. Explicit viscid fluxes $\overline{F}^n_{\mathrm{v}}$. For the evaluation of the explicit viscid fluxes in the x-momentum equation at the $(i+\frac{1}{2})$ face, i.e., $\sum_{\text{faces}} \overline{F}^n_v$ (see Eq. (10)), we only account for the contribution of the gradient in the x-direction over a shifted control volume surrounding a cell $P_{i+1,j,k}$ (see Fig. 4). It is referred to as the principal direction due to dropping its cross-derivative. In fact, this is equivalent to a common simplification like the so-called thin shear layer (TSL) approximation. With a central difference scheme, hence, one can obtain

$$\begin{aligned}\frac{1}{V}\left(\overline{F}^n_v\right)_{i+\frac{1}{2}} &= \frac{v_{\text{eff}}}{V}\left\{\left(\frac{\partial\varphi}{\partial x}n_x+\frac{\partial\varphi}{\partial y}n_y+\frac{\partial\varphi}{\partial z}n_z\right)S\right\}_{i+\frac{1}{2}} = \frac{v_{\text{eff}}S_{i+\frac{1}{2}}}{V\tilde{V}}\sum_{\text{faces}}\left(n_x\tilde{n}_x+n_y\tilde{n}_y+n_z\tilde{n}_z\right)\varphi\tilde{S}\\ &= \frac{v_{\text{eff}}S_{i+\frac{1}{2}}}{V\tilde{V}}\left\{\left(\varphi\tilde{S}\right)_{i+1}-\left(\varphi\tilde{S}\right)_i\right\} = \frac{v_{\text{eff}}}{d_i\Delta x}\left(\varphi_{i+1,j,k}-\varphi_{i,j,k}\right)\end{aligned} \tag{28}$$

according to Eq. (15). The subscripts $(i, i+1)$ stand for the cell faces of a shifted control volume with the face area $\tilde{S}$ surrounding the volume $\tilde{V}$ (see Fig. 4), respectively. $\Delta x = \frac{\tilde{V}}{\tilde{S}}$ (see Fig. 4) and $d_i^{-1} = \frac{S_{i+\frac{1}{2}}}{V}$ (see Fig. 3) are the corresponding thickness of a cell, respectively. $n_x\tilde{n}_x + n_y\tilde{n}_y + n_z\tilde{n}_z = 1$ in this case. It is obvious that Eq. (16) and the pressure Poisson equation of Eq. (22) can be derived in a manner similar to the above procedure.

2.2.6. An artificial damping term

The normal face velocity u_n (see Eq. (12)) at a certain face is obtained by

$$(u_n)_{i+\frac{1}{2}} = \frac{1}{2}\left\{(u_n)_i + (u_n)_{i+1}\right\} - d_{i+\frac{1}{2}} \tag{29}$$

for the evaluation of the volumetric flux $\dot{M}_{i+\frac{1}{2}}$ at $(i+\frac{1}{2})$ face. $(u_n)_i$ and $(u_n)_{i+1}$ are the values of the normal velocity at cells (i) and $(i+1)$ (see Fig. 3), respectively. $d_{i+\frac{1}{2}}$ is the so-called damping terms introduced at the corresponding face.

The linear interpolation of the face value is of a second-order accuracy (with central differencing) but results in an unbounded solution for problems of the convective domination. Owing to lack of numerical dissipation, high-order upwind schemes may lead to unphysical oscillations at high Reynolds number. To cope with such problems, one approach is to apply van Leer's limiter for the fluxes [56]. Alternative is to introduce the artificial dissipation terms that may remove the high frequency oscillations and prevent the occurrence of unphysical situation around discontinuities [16], which acts as a blend of 2nd and 4th order artificial dissipations in terms of the velocity [20], where the corresponding two constants $k^{(2)}$ and $k^{(4)}$ are fixed equal to 1.0 and 0.03 [11], respectively. Probably, a popular way is the momentum-based interpolation [41] that may be derived as an expression similar to 4th order artificial dissipation with respect of the pressure. In this study, we absorb an idea like a combination of the second- and fourth-order artificial dissipation terms but it is concerned with the pressure rather than the velocity. Furthermore, it corrects directly the normal face velocity u_n (see Eq. (29)), which makes a code more compact in writing. The major benefit is that it can suppress the oscillatory behaviour in regions with the sharp gradients (such as near

shocks) and damp the numerical disturbance induced by short wavelengths. Consequently, numerical stability can be enhanced.

We design $d_{i+\frac{1}{2}}$ as the compact form in terms of variables (i.e., the pressure) of the right (R) and left (L) sides at a certain face. Namely

$$d_{i+\frac{1}{2}} = \frac{1}{2\rho\psi_2 c_2}\left(p^R_{i+\frac{1}{2}} - p^L_{i+\frac{1}{2}}\right)_1 - \frac{1}{2\rho\psi_4 c_4}\left(p^R_{i+\frac{1}{2}} - p^L_{i+\frac{1}{2}}\right)_3, \tag{30}$$

which represents a blend of the second- and fourth-order artificial damping terms at the face $(i+\frac{1}{2})$. The subscripts $(1,3)$ imply the use of an one-order upwind (see Eq. (27)) and a third-order upwind scheme (see Eq. (25)) for achievement of values of the left and the right at the $(i+\frac{1}{2})$ face, respectively. Generally, the first- and third-derivative terms in the pressure (see Eq. (30)) add numerical dissipations similar to those created by the second- and fourth-order dissipation terms. Moreover, the high-order scheme may adjust amount of the numerical diffusion induced by the low-order scheme like the flux-corrected transport (FCT) algorithms [62], when it is active as an anti-diffusive term. Both become negligible with the smooth pressure fields but suppress oscillations in the region of the strong pressure gradients, because of their high-frequency damping capability. In our study, the corresponding coefficients that control the artificial dissipation (see Eq. (30)) are given adaptively in terms of the velocity, the local time step and the diagonal coefficients, except for $c_2 = 1$ be enforced artificially.

2.2.6.1. A choice of ψ_2 and ψ_4. ψ_2 or ψ_4 is of the same order as the velocity fields. Consequently, one can scale with a local velocity for ψ_4:

$$\psi_4 = \frac{\min(\Delta x, \Delta y, \Delta z)}{\Delta t},$$

where $(\Delta x, \Delta y, \Delta z)$ are the thickness of a cell in the x-, y- and z-directions (see Fig. 4), respectively.

Alternative is to consider the local diffusion velocity $\frac{v_{\text{eff}}}{\Delta d}$, in case it becomes important [33]. Namely

$$\psi_2 = u_{\max} + v_{\text{w}} + 2\frac{v_{\text{eff}}}{\Delta d},$$

where $u_{\max}$ is the maximum velocity within the flowfield at each time step. In the present case, it is essential to take into account the contribution from motions of the waves, indicating that the velocity of the wave train v_{w} (see Eq. (47)) should be incorporated $\Delta d = (\Delta x^2 + \Delta y^2 + \Delta z^2)^{1/2}$.

2.2.6.2. Determination of c_2 and c_4. For the two non-dimensional coefficients c_2 and c_4, a simple way is to set as $c_2 = 1$ and $c_4 = 1 + (A_p^{(1)} - 1) + (A_p^{(2)} - 1) + (A_p^{(3)} - 1)$, respectively. Actually, the latter is given as the diagonal coefficients from Eq. (17).

To investigate the numerical behavior of the damping terms (see Eq. (30)), one way is to discuss the local diffusion velocity $\frac{v_{\text{eff}}}{\Delta d}$ with varying v_{t} and v, based on $v_{\text{eff}} = v_{\text{t}} + v$. Obviously, this involves the effects of the SGS models and the Reynolds number, respectively. When using two different SGS models and increasing the Reynolds number, therefore, it is seen that the influence of v_{t} on the wave-induced flows is relatively large, as compared with that of v, as shown in Figs. 18 and 21.

2.3. Operator split advection algorithm for α

At each time step, interfaces over mixed cells are enforced to align with mesh coordinates, dependent on the local distributions of discrete α. This directly borrows the general idea of Hirt–Nichols's algorithm [17]. Its strength is of great simplicity for an interface reconstruction algorithm (named as a piecewise-constant

reconstruction of the interface), indicating that no explicit interface reconstruction is required in computations. We emphasize mainly, therefore, how to achieve α with the advection algorithm as follows.

2.3.1. An advection algorithm for α

Given an approximation to interfaces over mixed cells horizontally or vertically or both under the underlying velocity, the following advective equation is discretized within the whole computational domain:

$$\frac{\partial \alpha}{\partial t}+\frac{\partial(u\alpha)}{\partial x}+\frac{\partial(v\alpha)}{\partial y}+\frac{\partial(w\alpha)}{\partial z}=\alpha\left\{\frac{\partial u}{\partial x}+\frac{\partial v}{\partial y}+\frac{\partial w}{\partial z}\right\} \tag{31}$$

instead of Eq. (1). This is because the presence of the additional term (see Eq. (31)) captures the effects of individual derivatives, such as $\frac{\partial u}{\partial x}, \frac{\partial v}{\partial y}$ and $\frac{\partial w}{\partial z}$, in each spatial direction. Such consideration helps to achieve an accurate simulation, especially with an operator split advection algorithm, as illustrated in Fig. 5, where the calculated results look better, with the inclusion of $\nabla \cdot \vec{u}$. One reason may be explained as the fact that local and global volume-filling constraints are adhered to much more closely [2,42,47].

Using an explicit FV approach, this yields

$$\frac{\alpha^{n+1}-\alpha^{n}}{\Delta t}=-\frac{1}{V}\sum_{\text{faces}}\left(\dot{M}\alpha^{n}\right)+\frac{\alpha^{n}}{V}\sum_{\text{faces}}\dot{M}. \tag{32}$$

On the basis of a second-order explicit Adams–Bashforth formulation and the ADI algorithm, Eq. (32) is split as three one-dimensional equations as follows:

$$\begin{aligned}
\alpha^{(1)} &= \alpha^{n}-\frac{\Delta t}{V}\left(\frac{3}{2}\xi^{n}-\frac{1}{2}\xi^{n-1}\right),\\
\alpha^{(2)} &= \alpha^{(1)}-\frac{\Delta t}{V}\left(\frac{3}{2}\eta^{n}-\frac{1}{2}\eta^{n-1}\right),\\
\alpha^{n+1} &= \alpha^{(2)}-\frac{\Delta t}{V}\left(\frac{3}{2}\zeta^{n}-\frac{1}{2}\zeta^{n-1}\right)
\end{aligned} \tag{33}$$

in which ξ, η and ζ denote as, respectively,

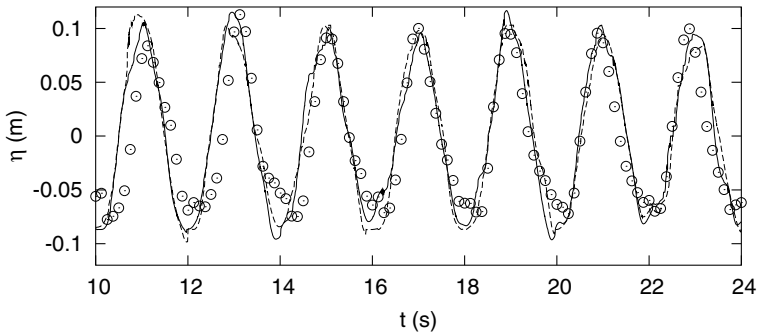

Fig. 5. Comparison with and without $\nabla \cdot \vec{u}$ for time history of the surface elevation at WG2 ($x = 2.02$ m) using grids (251×40) for a sea dike. (—) with $\nabla \cdot \vec{u}$; (– – –) without; (⊙) measurement.

$$\xi = \left(\dot{M}\alpha^n\right)_{i+\frac{1}{2}} - \left(\dot{M}\alpha^n\right)_{i-\frac{1}{2}} - \alpha^n\left(\dot{M}_{i+\frac{1}{2}} - \dot{M}_{i-\frac{1}{2}}\right),$$
$$\eta = \left(\dot{M}\alpha^{(1)}\right)_{j+\frac{1}{2}} - \left(\dot{M}\alpha^{(1)}\right)_{j-\frac{1}{2}} - \alpha^{(1)}\left(\dot{M}_{j+\frac{1}{2}} - \dot{M}_{j-\frac{1}{2}}\right),$$
$$\zeta = \left(\dot{M}\alpha^{(2)}\right)_{k+\frac{1}{2}} - \left(\dot{M}\alpha^{(2)}\right)_{k-\frac{1}{2}} - \alpha^{(2)}\left(\dot{M}_{k+\frac{1}{2}} - \dot{M}_{k-\frac{1}{2}}\right),$$

where $\alpha^{(1)}$ and $\alpha^{(2)}$ represent the corresponding values of α at the end of each sweeping fractional step, respectively. This involves the sweep in the x-direction for updating $\alpha^{(1)}$, and then followed the sweeps in $y-$ and $z-$directions, respectively, for updating $\alpha^{(2)}$ and α^{n+1}. Indices, $(j \pm \frac{1}{2})$ and $(k \pm \frac{1}{2})$, stand for the corresponding cell face in the $y-$ and $z-$directions (see Fig. 2), respectively. In addition, their iterative order in the x-, y- and z-directions is inverted to alleviate the introduction of the systematic error.

2.3.2. A weighted upwind and blending schemes

With the present Eulerian interface, the interfaces are allowed for arbitrary orientation with respect to the computational grid. Hence, the volume fluxes $\dot{M}$ at a certain face over mixed cells, for example, $\dot{M}_{i+\frac{1}{2}}$ at the face $(i+\frac{1}{2})$, can be expressed as

$$\dot{M}_{i+\frac{1}{2}} = (u_n S)_{i+\frac{1}{2}},$$

where S is the cell face area at the $(i+\frac{1}{2})$ face. Owing to $u_n = un_x + vn_y + wn_z$, the face velocities (u, v, w) at mixed cells need to be determined. As described in the Section 2.8.2, they may be achieved with the corresponding momentum equations or the tangential dynamic free-surface boundary conditions, dependent on the relation of α with its neighbouring cell. An essential point, therefore, is to evaluate the volume fraction $\alpha_{i+\frac{1}{2}}$ at the corresponding face in case the sharpness and the shape of the interface are maintained.

We attempt to apply high-order upwind schemes (such as the MUSCL scheme and the ENO one) for the evaluation of the value of $\alpha_{i+\frac{1}{2}}$ at the face $(i+\frac{1}{2})$. Unfortunately, both fail due to rapid generation of unphysical volume fraction α over several cells in the interior of the fluid. But with a hybrid approach that includes a weighted upwind scheme and a blending one, we found that it did well. Additionally, the corresponding code has to be developed in a compressive discretization manner, indicating that only the absolute fluxes across the face $(i+\frac{1}{2}), (j+\frac{1}{2})$ and $(k+\frac{1}{2})$, respectively, are involved, while the volume fractions at cell (i) and its neighbour are renewed simultaneously. In this way, the latter will be activated for achievement of $\alpha_{i+\frac{1}{2}}$ as long as one of its two neighbors becomes an empty cell having $\alpha = 0$. Otherwise, the former is active. Consequently, two separated approaches are constructed for the advection of a step profile of α, dependent of its distributions. In our study, the weighted upwind scheme consists of an one-order upwind differencing plus a high-order upwind one. It can guarantee a bounded solution, while a portion of high-order upwind fluxes is incorporated to counteract numerical diffusion created by the low-order upwind scheme [3]. On the other hand, the blending scheme helps to steepen the resolution of the interface when using an appropriately weighting coefficient [53].

For the calculation of an intermediate $\alpha^{(1)}$, for example, $\alpha_{i+\frac{1}{2}}$ at the face $(i+\frac{1}{2})$ is evaluated by

$$\alpha_{i+\frac{1}{2}} = \begin{cases} (1-\beta)\alpha_i^n + (1+\beta)\alpha_{i+1}^n & \text{if } \alpha_{i-1}^n \text{or } \alpha_{i+1}^n = 0, \\ \Gamma\alpha_i^n + (1-\Gamma)(-\alpha_{i+\frac{1}{2}}^{\mathrm{L}}) & \text{otherwise,} \end{cases} \tag{34}$$

when $\dot{M}_{i+\frac{1}{2}} \geqslant 0$. The subscripts $(i-1, i+1)$ represent two neighbours of cell (i), respectively, as illustrated in Fig. 3, in which the corresponding subscripts used are labelled. Γ stands for a flux-limiter that combines a high-order convective flux-function $\alpha_{i+\frac{1}{2}}^{\mathrm{L}}$, well behaved in the smooth region of flows, with a low-order one α_i^n, working well near the sharp gradients. According to general information on the resolved velocity fields, it is achieved with the monotone methods, which can actually be viewed large-eddy simulation models with

an intrinsic subgrid-scale algorithm. As a result, this leads to arise naturally from the nonlinear monotonicity preserving the flux limiting feature [8]. In this study, van Leer limiter [56] is introduced and it is given by

$$\Gamma = \max\{0.5, \min(\Gamma_1, \Gamma_2, 1.0)\} \tag{35}$$

indicating that the limiter involves as much as possible of the anti-diffusion term but without increase of the variation of the solution so that physical principals of monotonicity and positivity are complied with [3]. The coefficients (Γ_1, Γ_2) are expressed as, respectively,

$$\Gamma_1 = \frac{u_{\max} - \min\left(u_{i+\frac{1}{2}}, u_{\max}\right)}{\max\left(\epsilon, u^g_{\max} - u_{i+\frac{1}{2}}\right)}, \quad \Gamma_2 = \frac{\max\left(u_{i+\frac{1}{2}}, u_{\min}\right) - u_{\min}}{\max\left(\epsilon, u_{i+\frac{1}{2}} - u^g_{\min}\right)}.$$

To avoid zero divides, a very small value ($\varepsilon = 10^{-25}$) is used. It is clear that the velocities in any three neighboring cells are monotonic once the van Leer limiter Γ is restricted within $0.5 \leqslant \Gamma \leqslant 1$. Accordingly, the local minimum and maximum velocities $u_{\min}$ and $u_{\max}$ are set by $u_{\min} = \min(u_{i-\frac{1}{2}}, u_{i+\frac{3}{2}})$ and $u_{\max} = \max(u_{i-\frac{1}{2}}, u_{i+\frac{3}{2}})$, respectively, when $u^g_{\min} = \min(u^g_{i+1}, u^g_i)$ and $u^g_{\max} = \max(u^g_{i+1}, u^g_i)$, where u^g_{i+1} and u^g_i are obtained with the Taylor expansions:

$$u^g_{i+1} = u_{i+\frac{1}{2}} + \frac{1}{4}\left(u_{i+\frac{3}{2}} - u_{i-\frac{1}{2}}\right), u^g_i = u_{i+\frac{1}{2}} - \frac{1}{4}\left(u_{i+\frac{3}{2}} - u_{i-\frac{1}{2}}\right)$$

according to a central-difference discretization for the derivative $(\frac{\partial u}{\partial x})_{i+\frac{1}{2}}$. Naturally, the value at the face $(i+\frac{1}{2})$ always takes its left state $\alpha^{\mathrm{L}}_{i+\frac{1}{2}}$ due to the presently compressive discretization manner, which may be evaluated with the ENO scheme (see Eq. (26)). The weighting factor β is expressed by

$$\beta = \frac{\alpha^{\mathrm{u}} - \tilde{\alpha}_i}{1 - \tilde{\alpha}_i}.$$

This is a simplified case relative to the original one with the different blending scheme used [53]. α^u and $\tilde{\alpha}_i$ are given by, respectively,

$$\alpha^{\mathrm{u}} = \min\left(\frac{\tilde{\alpha}_i}{c}, 1\right) \quad \text{and} \quad \tilde{\alpha}_i = \frac{\alpha^n_i - \alpha^n_{i-1}}{\alpha^n_{i+1} - \alpha^n_{i-1}},$$

where c is a constant ($c = 0.2$ in this case) and the last term on the right of Eq. (32) is taken away. Finally, $\alpha^{(2)}$ is estimated and then α^{n+1} at the next time step is renewed, which is analogous to the process described above. Due to round-off error, the volume fraction α may vary slightly below 0 or above 1. To circumvent any error in α, we truncate α as follows:

$$\alpha^{n+1}_i = \begin{cases} 0 & \text{if } \alpha^{n+1}_i \leqslant 0, \\ 1 & \text{if } \alpha^{n+1}_i \geqslant 1 \end{cases}$$

for the numerical overshoot and undershoot.

This procedure can be made second-order simply by alternating the sweep direction at each time step. Its advantage lies in that this approach is simple (easy to write a source code) and effective because it can keep the front sharp and provide such desirable properties during tracking the interfaces. By comparison, the original VOF method [17] gives incorrect information in the surf zone, where the fluid film on the slope tends to be too thick, as illustrated in Fig. 6. But the current approach captures well this one, which is confirmed by comparison with measurements available. In particular, two state motions, for example, at $t = 17.0$ and 33.0 (s) almost maintain to be periodic, indicating that our computations are stable.

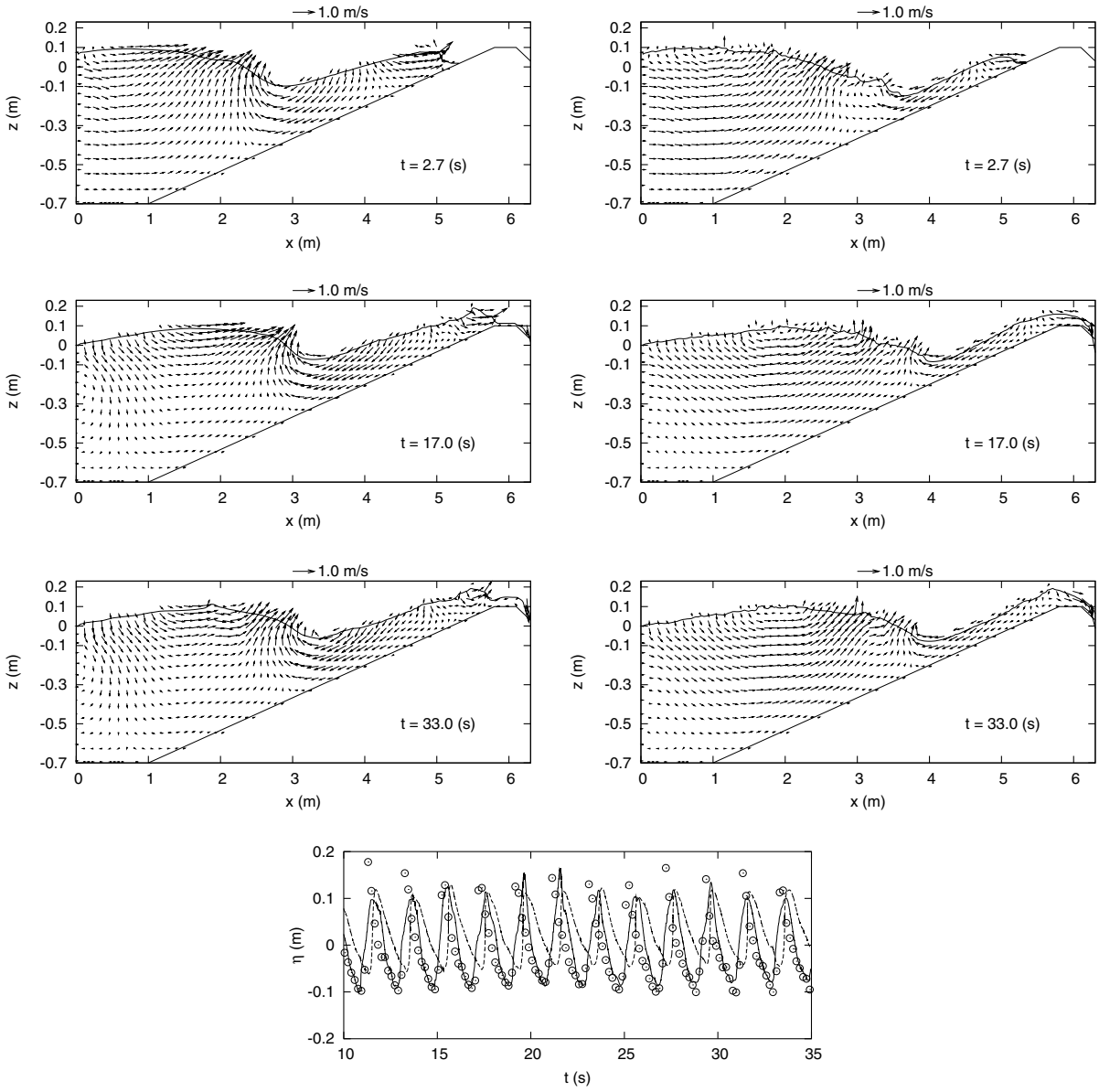

Fig. 6. Comparison of the present approach (right) with the original VOF method (left) for the wave-induced velocity field and the surface elevation versus time at one point ($x = 3.81$ m) with grids (251×40) for a sea dike. (—) the present approach; (– – –) the original VOF approach; (⊙) measurement.

2.4. A subgrid-scale model

In the context of conventional LES, a Smagorinsky-type isotropic eddy-viscosity model is widely applied, for example, in the field related to the free-surface [6,59], where the effects of the SGS stresses are considered in a statistical sense only. Theoretically, its use tends to be diffusive in the course of the process

that has dissipated a portion of its kinetic energy into the turbulent energy. With this model, an attractive benefit is without the need of the boundary conditions at the free surface specified.

According to Smagorinsky's model [48], the eddy viscosity v_t is evaluated by

$$v_t = C_s(l_v\Delta)^2|\bar{S}|, \tag{36}$$

where C_s is Smagorinsky's constant ($C_s = 0.01$ in this case), Δ is a characteristic length scale of the small eddies given by $\Delta = \min(\Delta x, \Delta y, \Delta z)$, which is slightly different from the formulation adopted in the original Smagorinsky's model, $\Delta = (\Delta x\Delta y\Delta z)^{1/3}$, and $|\bar{S}| = \sqrt{2\bar{S}_{ij}\bar{S}_{ij}}$ $(i,j = 1,2,3)$ with the strain rate tensor S_{ij} defined as $S_{ij} = \frac{1}{2}(\frac{\partial u_i}{\partial x_j} + \frac{\partial u_j}{\partial x_i})$. Since the subgrid eddy-viscosity will reduce to zero in the vicinity of the wall, the so-called van Driest damping function l_v ($l_v = 1 - e^{-\frac{y^+}{26}}$ instead of $l_v = 1$) is employed, when approaching the wall. The nondimensional distance y^+ can be written as $y^+ = d\frac{u_\tau}{v} = d\frac{\sqrt{\tau/\rho}}{v} = d\{\frac{|\nabla\times\vec{V}|}{v}\}_w^{1/2}$, where d is the distance normal to the wall, u_τ is the friction velocity ($u_\tau = \sqrt{\tau/\rho}$, τ is the stress acting on a wall) and $\vec{V} = u\vec{i} + v\vec{j} + w\vec{k}$. The subscript w stands for the wall. As expected, the eddy viscosity v_t is calculated once the final velocity is available at each time step.

2.5. A local time step Δt

A local time step Δt involves the variation of the flow and the subgrid spacing. Normally, it may be determined on the basis of the so-called Courant–Friedrichs–Lewy (CFL) constraint, dependent on the various options: the convective and viscous terms together with the stiff source terms (e.g., gravity and surface tension force).

To obey the CFL conditions, a common way to define a local time step Δt_1 for the inviscid fluxes is

$$\Delta t_1 = \frac{1}{2}\frac{V}{|\dot{M}_{i+\frac{1}{2}}| + |\dot{M}_{j+\frac{1}{2}}| + |\dot{M}_{k+\frac{1}{2}}| + c|\dot{M}_w|}\mathrm{CFL}$$

by setting CFL = 0.3. An additional feature in this expression is to involve the wave fluxes expressed by

$$\dot{M}_w = v_w S, S = \left(S^2_{i+\frac{1}{2}} + S^2_{j+\frac{1}{2}} + S^2_{k+\frac{1}{2}}\right)^{1/2},$$

where v_w is the celerity of the incident wave determined by a linear wave theory (see Eq. (47)), and the constant c ($c = 10$ in this case) is introduced in order to enhance the stability in computations. Some reasons may be attributed to the fact that the presence of the gravitational term requires a more restrictive time step in the fluids initially at rest, especially when Eq. (31) for α is resolved.

Owing to the presence of the viscous fluxes, the time step Δt_2 is evaluated as

$$\Delta t_2 = \frac{d^2}{4v}, \quad d = \frac{V}{\max\left(S_{i+\frac{1}{2}}, S_{j+\frac{1}{2}}, S_{k+\frac{1}{2}}\right)}.$$

Under the surface tension effects, on the other hand, the time step Δt_3 is given as

$$\Delta t_3 = \left(\frac{\rho V}{4\pi\sigma}\right)^{1/2}.$$

Thus, the finial time step Δt will depend on their minimum values:

$$\Delta t = \min(\Delta t_1, \Delta t_2, \Delta t_3).$$

2.6. A cut-cell Cartesian technology

With TDMA and ICCG, the resulting matrix equations for the Delta form and the pressure should be resolved on each cell in the whole computational domain, regardless of whether a cell represents fluid, mixed, void or an obstacle that involves with and without a cut boundary (see Fig. 7 for five types of cells). It is no problem to find the solution over a fluid, cut or mixed cell. However, singularities occur in "bad" cells such as void and whole obstacle cells, where ρ is zero for the former and undefined for the latter. One approach to avoid such a problem is to enforce a considerable value to the mainly diagonal coefficients in the linear equation (see Eqs. (17) and (22)), when the sweep points to the bad cells. With the well-conditioned matrices (such as diagonal dominant), it can be shown that both algorithms will always converge. For Eq. (17), for example, by multiplying the diagonal coefficients $(A_{i-1}, A_p^{(1)}, A_{i+1})$ with a very large value relative to ∞ and zero over the bad cells, respectively, one has

$$\widehat{A}_{i-1} = A_{i-1} \times \text{zero}, \quad \widehat{A}_p^{(1)} = \text{coef}, \quad \widehat{A}_{i+1} = A_{i+1} \times \text{zero}, \quad \widehat{R} = R \times \text{zero},$$

where coef $= 1.0 \times 10^{25}$ and zero $= 0$. Additionally, void and whole obstacle cells are thought as internal Dirichlet and Neumann boundaries, respectively. Hence, the coefficients have to be rearranged in the operator matrix by manipulating the corresponding elements according to Dirichlet and Neumann boundaries, once the neighbour adjacent a computational cell becomes the bad cells.

On the other hand, the effect of a structure over a cut cell is incorporated through the introduction of variables that represent an effective geometry space covered a fluid. Also, arbitrarily small cut cells are treated carefully, especially when decreasing mesh size. Owing to the current implicit approach, the presence of small cells near a wall seems not to restrict the time step. Only the pressure over such cells is handled with a mirror symmetry, because it is located at the center of a cell. Additionally, the pressure and α at the intersection of a free surface with a wall are also evaluated in the same way.

2.7. Flowchart of the current approach

With a staggered-grid arrangement, a cut-cell implicit finite volume VOF approach is applied for resolution of the NS equations with interfaces, provided that the initial conditions and all the boundary

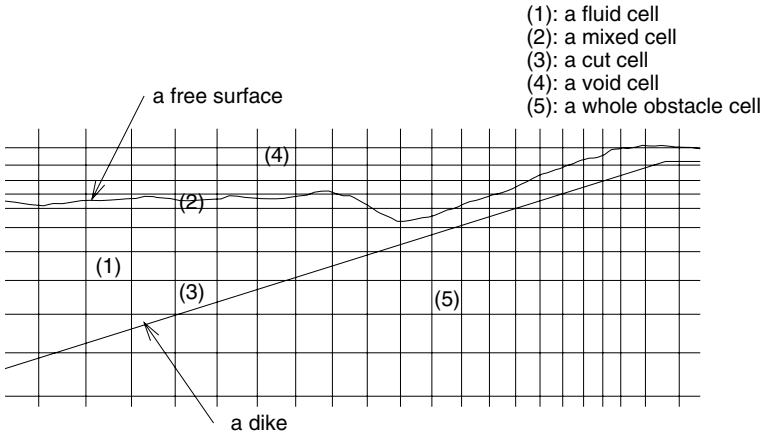

Fig. 7. Denotaton of five types of cells over a Cartesian cut-cell mesh.

conditions are given explicitly. The computational flowchart of the present solver is illustrated in Fig. 8, which displays that the solution is advanced in time. The following is to describe its major procedure.

With the ENO scheme (Eq. (26)), the corresponding face values are estimated, which may be used for achievement of the inviscid fluxes by means of the flux-difference splitting approach (Eq. (24)), while the explicit viscous fluxes are evaluated with a central-difference scheme according to Eq. (28). Given the explicit fluxes, the Delta form of the velocity is updated through ADI factorization with a local time step (Eq. (17)). This defines a temporal velocity under the surface tension effects (Eq. (18)). Consequently, the pressure can be realized with a projected algorithm according to the velocity distributions. Finally, the volume fraction α is achieved with the help of the final velocity (Eq. (23)) at the end of the outer iteration. When approaching the normal face velocity, a blend of the second- and fourth-order artificial damping terms is activated, where the MUSCL scheme (Eq. (25)) is employed for discretization of the third-order derivative terms.

To deal with an arbitrary geometry, a cut-cell treatment technology over a fixed mesh is implemented. A few parameters in the INPUT file (such as the period, the wave evaluation and the grid numbers together with a running time) are specified by a user. Each outer iteration only repeats three times but during the inner iteration, iterative number for the pressure is completely dependent on the residual norm less than a given error tolerance ε ($\varepsilon = 10^{-8}$ in this case) based on the ICCG method. Note that the solution of the discretizated pressure Poisson equation is the most time-consuming part. It is shown that the number will

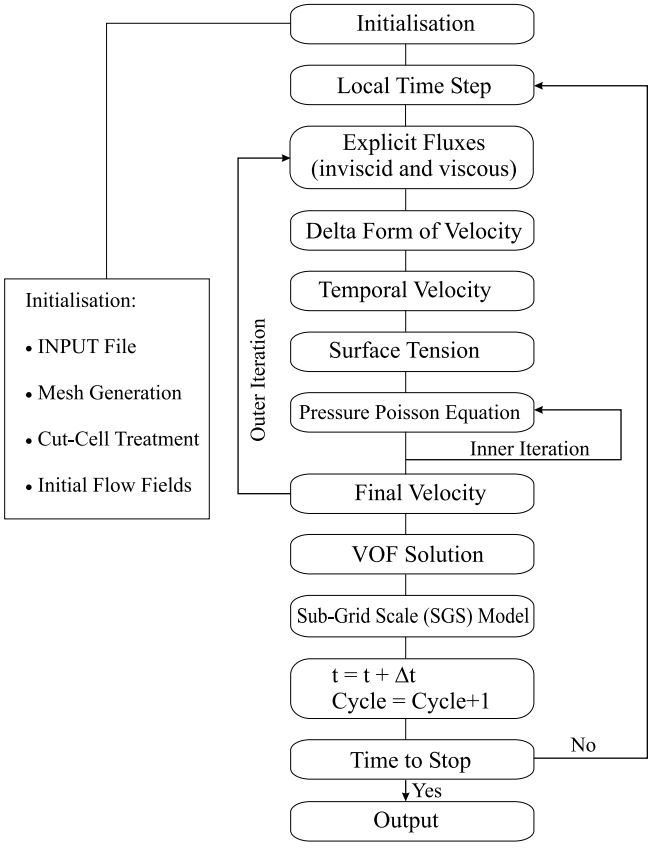

Fig. 8. Flowchart of the present algorithmic steps.

significantly increase with respect to mesh refinement. The description in more detail can be found in our current work [28].

2.8. Initial and boundary conditions

2.8.1. Initial conditions

All simulations started from complete rest so that the unsteady motion characteristics of waves evolved naturally. At $t = 0$, $u = v = w = 0$, and the volume fractions α (an indicator function $\alpha(\vec{r}, t), \vec{r} = x, y, z$) are initially assigned by

$$\alpha(\vec{r}, t) = \begin{cases} 1, & \text{in the fluid,} \\ \alpha, & \text{over mixed cells,} \\ 0, & \text{in a void} \end{cases}$$

with respect to SWL, where α over mixed cell is calculated by Eq. (46). The hydrostatic pressure is used as an initial state for the pressure. This is a most general situation in a numerical (or physical) wave tank, as illustrated in Fig. 9 for free-surface configurations starting from the initial stage (a flat at $t = 0$) to the first period $T = 2$ (s). At the beginning, an initially flat free surface is perturbed by imposing a wavemaker placed at the inlet. As time progresses, the waves propagate towards a dike at $t = 0.5$ (s). After that, the wave shape tends to be asymmetric at $t = 1.0$ (s) until the amplitude varies slightly at $t = 2$ (s), as compared with that at $t = 1.5$ (s).

2.8.2. Boundary conditions

For the pressure, it is unnecessary to specify the boundary conditions with the ICCG algorithm, except at the free surface. The wall effect is incorporated by enforcing the slip boundary conditions for a cut cell or no-slip conditions for a mesh boundary. At the free surface, the viscous effect is ignored but surface tension is modelled with a localized volume force by the CSF model. It leads to simplify the normal dynamic free-surface boundary condition:

$$p = 0 \tag{37}$$

at a free surface. To comply with this condition over mixed cells, the matrix of the pressure Poisson equation in the x–z plane is dealt with by setting the corresponding coefficient to zero. According to Eq. (22), the matrix M for each cell is expressed as

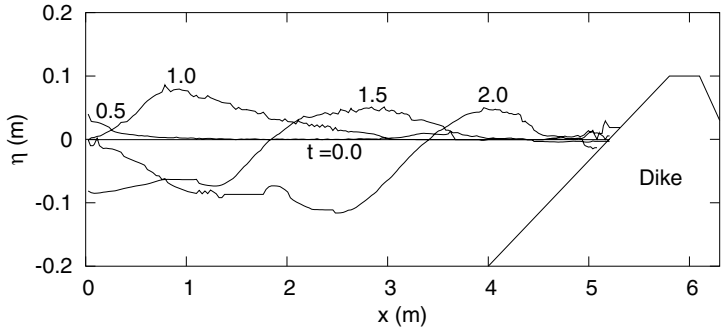

Fig. 9. Development of waves from its initial stage $t = 0$ to the first period $T = 2$ (s) (magnified view) with grids (251×40).

$$M = \begin{pmatrix} 0 & D^{u}_{i,j,k+1} & 0 \\ B^{l}_{i-1,j,k} & A_{i,j,k} & B^{u}_{i+1,j,k} \\ 0 & D^{l}_{i,j,k-1} & 0 \end{pmatrix}, \tag{38}$$

where A to D are diagonals with functions of the metric terms and the density, dependent on the actual grid distribution (that is, the cell thickness and the corresponding face area). When a cell at $(i, j, k+1)$ becomes an empty cell (see Fig. 10), for example, the main diagonal A and the diagonal $D^{u}_{i,j,k+1}$ in the matrix M with its nearest neighbors (that is, all neighbor shares one face in Eq. (38)) are arranged with

$$A^{*}_{i,j,k} = A_{i,j,k} - D^{u}_{i,j,k+1} \quad \text{and} \quad D^{u}_{i,j,k+1} = 0 \tag{39}$$

during the inner iteration. The treatment is quite simple without the need for the extrapolated pressure like the so-called irregular star [5] or the weighted length interpolation [17] over mixed cells.

Instead of the use of the momentum equation, the corresponding three components of the velocities over mixed cells (or void cells adjacent to mixed cells) may be extrapolated with the gradients of the zero-normal velocity from the interior of the flow:

$$\frac{\partial \varphi}{\partial n} = 0, \quad \varphi = (u, v, w)$$

once its neighbour is an empty cell. n is the component normal to the free surface. This is the so-called inviscid tangential dynamic free-surface boundary conditions under negligence of the surface viscosity [26]. Since $w_{i,j,k}$ etc. are calculated with the momentum equation, only the velocity $u_{i,j,k}$ over mixed cells exposed to the air (see Fig. 10), for example, is enforced by the continuity equation but $u_{i,j,k+1}$ is evaluated with the mirror approach: $u_{i,j,k+1} = u_{i,j,k}$.

2.8.3. Surface tension

With the CSF model, surface tension is formulated as a localized volume force $\vec{F}_{sv}$ that accounts for the curvature-dependent interfacial effects. Without the need of detailed interface information, it was incorporated to the source term in the momentum equations (see Eq. (6)), while acting on the fluid elements lying within the finite thickness transition region. In this sense, therefore, a body force defined at the centre of a cell (see Fig. 11) is given by

$$\vec{F}_{b} = \vec{F}_{sv} = \sigma \kappa \vec{m}, \tag{40}$$

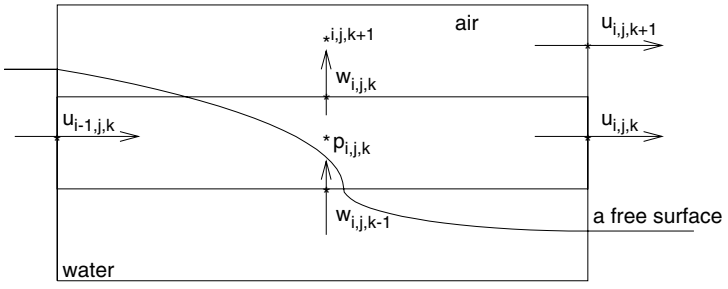

Fig. 10. Implementation of the tangential dynamic free-surface boundary conditions. (i, j, k) and $(i, j, k+1)$ represent cells, respectively.

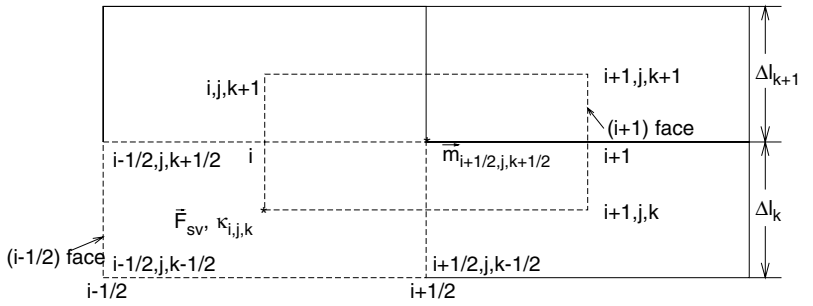

Fig. 11. Denotation of a body force $\vec{F}_{\mathrm{sv}}$, curvature κ and normal $\vec{m}$ over a cell. $(\vec{F}_{\mathrm{sv}}, \kappa)$ are defined at the center of a cell (i, j, k), respectively; and $\vec{m}$ defined at the vertex $(i + 1/2, j, k + 1/2)$ of a cell (i, j, k). $(i - 1/2, i + 1/2)$ and $(i, i + 1)$ denote the corresponding cell faces, respectively.

where the surface tension coefficient σ is set as a constant. κ and $\vec{m} = (m_x, m_y, m_z)$ are the cell-centred curvature of a free surface and a normal vector at the vertex $(i + \frac{1}{2}, j, k + \frac{1}{2})$, respectively, as illustrated in Fig. 11,

$$\kappa = -\left(\nabla \cdot \frac{\vec{m}}{|\vec{m}|}\right) = \frac{1}{|\vec{m}|}\left\{\left(\frac{\vec{m}}{|\vec{m}|} \cdot \nabla\right)|\vec{m}| - \left(\nabla \cdot \vec{m}\right)\right\}$$

and

$$\vec{m} = \nabla\alpha.$$

Since κ is a function with the second-order spatial derivatives of α, it is dependent strongly on small error in α. This makes computations with surface tension more difficult, especially under breaking waves. To mitigate the high wavenumber contributions to κ, α has to be filtered when calculating local curvatures [4]. In this way, a blend of α and ρ is enforced to mollify by

$$\begin{aligned}(\widetilde{\alpha\rho})_{i,j,k} = {} & \frac{36}{64}(\alpha\rho)_{i,j,k} + \frac{6}{64}\left\{(\alpha\rho)_{i+1,j,k} + (\alpha\rho)_{i,j,k+1} + (\alpha\rho)_{i-1,j,k} + (\alpha\rho)_{i,j,k-1}\right\} \\ & + \frac{1}{64}\left\{(\alpha\rho)_{i+1,j,k+1} + (\alpha\rho)_{i-1,j,k+1} + (\alpha\rho)_{i-1,j,k-1} + (\alpha\rho)_{i+1,j,k-1}\right\},\end{aligned}$$

where the subscripts represent a cell (i, j, k) and its 8 surrounding neighbours. Additionally, the value of the derivative $\frac{\partial m_x}{\partial x}$ at the centre of this cell is evaluated by a FV method

$$\begin{aligned}\left(\frac{\partial m_x}{\partial x}\right)_{ijk} &= \frac{1}{V}\sum_{\text{faces}} m_x n_x S \\ &= \frac{1}{V}\left\{(m_x n_x S)_{i+\frac{1}{2}} - (m_x n_x S)_{i-\frac{1}{2}}\right\} + \frac{1}{V}\left\{(m_x n_x S)_{j+\frac{1}{2}} - (m_x n_x S)_{j-\frac{1}{2}}\right\} \\ &\quad + \frac{1}{V}\left\{(m_x n_x S)_{k+\frac{1}{2}} - (m_x n_x S)_{k-\frac{1}{2}}\right\}\end{aligned}$$

with the face value $(m_x)_{i+\frac{1}{2}}$ at the face $(i + \frac{1}{2})$

$$(m_x)_{i+\frac{1}{2}} = \frac{1}{2}\left\{(m_x)_{i+\frac{1}{2},j,k+\frac{1}{2}} + (m_x)_{i+\frac{1}{2},j,k-\frac{1}{2}}\right\},$$

where m_x is the x component of the normal vector $\vec{m}$. It is computed by

$$(m_x)_{i+\frac{1}{2},j,k+\frac{1}{2}} = \left(\frac{\partial \alpha}{\partial x}\right)_{i+\frac{1}{2},j,k+\frac{1}{2}} = \frac{1}{V}\sum_{\text{faces}} \alpha n_x S$$
$$= \frac{1}{V}\left\{(\alpha n_x S)_{i+1} - (\alpha n_x S)_i\right\} + \frac{1}{V}\left\{(\alpha n_x S)_{j+1} - (\alpha n_x S)_j\right\} + \frac{1}{V}\left\{(\alpha n_x S)_{k+1} - (\alpha n_x S)_k\right\}.$$

As shown in Fig. 11, the subscripts $(i-\frac{1}{2}, i+\frac{1}{2})$ and $(i-1, i+1)$ represent the corresponding cell faces, respectively. Furthermore, the face value $(\alpha)_{i+1}$ at the face $(i+1)$ is obtained with a linearly weighted approach. Namely

$$(\alpha)_{i+1} = \frac{\alpha_{i+1,j,k+1}\Delta l_k + \alpha_{i+1,j,k}\Delta l_{k+1}}{\Delta l_k + \Delta l_{k+1}}.$$

Thus, the body force at the centre of a cell can be achieved once the cell-centred normal is available with the average of the vertex normal (see Fig. 11)

$$\vec{m}_{ijk} = \frac{1}{4}\left(\vec{m}_{i+\frac{1}{2},j,k+\frac{1}{2}} + \vec{m}_{i+\frac{1}{2},j,k-\frac{1}{2}} + \vec{m}_{i-\frac{1}{2},j,k+\frac{1}{2}} + \vec{m}_{i-\frac{1}{2},j,k-\frac{1}{2}}\right).$$

2.8.4. An absorbing-generating boundary condition

Many of absorbing boundaries [23,39,52] placed at the inlet are based on the assumption of the linear superposition of incident and reflected waves at the wave generating-absorbing boundary. A particular generator is an internal wavemaker that acts as a source function inside the computational domain [31]. Following the usual approach, we attempt to apply the so-called weakly reflecting boundary condition [36], which generates the incident waves and absorbs the weakly reflected waves simultaneously. Namely

$$\frac{\partial \varphi_r}{\partial t} - c\frac{\partial \varphi_r}{\partial x} = 0, \tag{41}$$

where $\varphi = (u, v, w, \eta)$. The wave celerity c is estimated by $c = \sqrt{gd}$ with the finite water depth d. The subscripts (t, r, i) used represent the total, reflected and incident waves, respectively.

Based on the assumption of the linear waves, the total waves are related to the incident waves via $\varphi_r = \varphi_t - \varphi_i$. This leads to Eq. (41) as

$$\frac{\partial \varphi_t}{\partial t} - c\frac{\partial \varphi_t}{\partial x} = \frac{\partial \varphi_i}{\partial t} - c\frac{\partial \varphi_i}{\partial x}, \tag{42}$$

which forms the so-called absorbing-generating boundary condition for a wave generator fixed at the inlet. According to the linear wave theory, the evaluation of the source terms in the right hand of Eq. (42) is straightforward for regular waves, once the three components (u, v, w) of the velocity at one ghost cell are given by

$$\begin{aligned} u_i &= \frac{H}{2} gT \frac{\cosh\{k(\eta_i + d)\}}{\lambda \cosh(kd)} \cos\left\{k\left(x + \frac{\lambda}{4}\right) - \omega t\right\}, \\ v_i &= 0, \\ w_i &= \frac{H}{2} gT \frac{\sinh\{k(\eta_i + d)\}}{\lambda \cosh(kd)} \sin\left\{k\left(x + \frac{\lambda}{4}\right) - \omega t\right\}. \end{aligned} \tag{43}$$

Since the particle moves periodically in the vertical direction around the origin, the phase departure $\frac{\lambda}{4}$ has to be incorporated to the corresponding phase function, as illustrated in Eqs. (43) and (44), where the surface elevation η_i with respect to SWL is obtained by

$$\eta_i = \frac{H}{2}\cos\left\{k\left(x+\frac{\lambda}{4}\right)-\omega t\right\}. \tag{44}$$

For the time integration of Eq. (42), a second-order explicit Adams–Bashforth formulation is implemented as follows (for example, $\varphi = \eta_t$):

$$\eta_t^{n+1} = \eta_t^n + \Delta t\left(\frac{3}{2}R^n - \frac{1}{2}R^{n-1}\right) = \eta_t^n + \Delta t R^n + \frac{\Delta t}{2}\left(R^n - R^{n-1}\right) \tag{45}$$

with the residual R defined by

$$R = \left(c\frac{\partial \eta_t}{\partial x} + \frac{\partial \eta_i}{\partial t} - c\frac{\partial \eta_i}{\partial x}\right).$$

For the first term, $c\frac{\partial \eta_t}{\partial x}$, for example, it is calculated by

$$c\frac{\partial \eta_t}{\partial x} = \frac{c}{V}\sum_{\text{faces}} \eta_t n_x S = \frac{c}{V}\left\{(\eta_t n_x S)_{i+\frac{1}{2}} - (\eta_t n_x S)_{i-\frac{1}{2}}\right\} = \frac{n_x c S}{V}\left\{\eta_{t_{i+\frac{1}{2}}} - \eta_{t_{i-\frac{1}{2}}}\right\},$$

where the values of $\eta_{t_{i+\frac{1}{2}}}$ and $\eta_{t_{i-\frac{1}{2}}}$ at a certain face are evaluated with an one-order upwind scheme (see Eq. (27)), respectively. Given the wave characteristics (see Table 1), the total waves η_t at the inlet are generated by the solution of Eq. (45), as illustrated in Fig. 12, where the effects of the reflected waves η_r on the incident ones η_i (see Eq. (44)) can be observed. Consequently, this yields α over one mixed cell given by

$$\alpha = \frac{\widetilde{V}}{V} = \frac{\eta_t + d - z_{k-1}}{\Delta l_k}, \tag{46}$$

where $\widetilde{V}$ is the wet volume, and Δl_k and z_{k-1} are the grid size and the coordinate in the vertical direction, respectively (see Fig. 11). Similar expression holds for $\varphi = (u, v, w)$ at the inlet together with the application at the outlet by setting $\varphi_i = 0$ in Eq. (42). The wave number k, the angular pulsation ω and the phase velocity v_w are defined as, respectively,

$$k = \frac{2\pi}{\lambda}, \quad \omega = \frac{2\pi}{T} \quad \text{and} \quad v_w = \frac{\lambda}{T}. \tag{47}$$

Using the linear wave theory, the wavelength λ is obtained by the following dispersion relationship:

$$\lambda = \frac{gT^2}{2\pi}\tanh(kd).$$

To reduce the generation of non-physical high-frequency waves, an adjustment function is implemented for both the wave elevation and the velocity at the inlet. It smoothly increases to unity at $t = 1.5$ (s) from its initial value of zero (see Fig. 12).

Table 1
The wave height H, the period T, the wavelength λ and the water depth d

H (m)	T (s)	λ (m)	d (m)
0.16	2.0	4.62	0.7

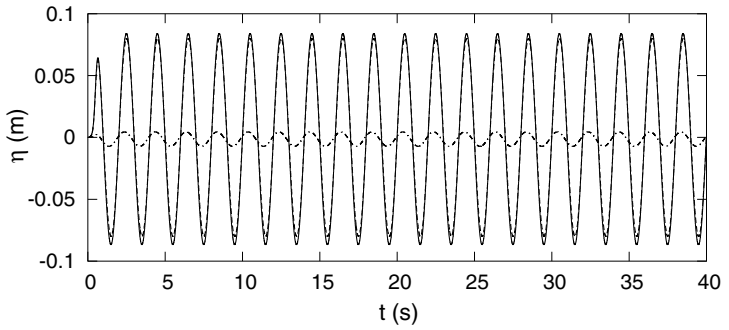

Fig. 12. Development of linear waves created by a wave generator, located at the inlet WG0 ($x = 0$). (—) the total waves; (– – –) the incident waves; (– · –) the reflected waves.

It is clear that Eq. (45) can be regarded as an one-order forward Euler scheme plus the modification of the current and previous residuals. It is the weakly reflecting boundary condition. One problem is that we adopt a single wave train (i.e., with one wave celerity) for an approximation of motions induced by the wave groups [12]. Generally, an effective approach at the open boundary is to combine the open boundary condition (e.g., Orlanski's condition) with a numerical damping approach (e.g., the sponge layer method [19]). We tested this case but implement a blend of the artificial damping terms of Eq. (30) and the Orlanski's open boundary condition (see Eq. (42)). Additionally, we also apply the mirror condition at the outlet instead of Eq. (45). Both computations are stable, indicating that the damping terms used work well due to its adaptive performance dependent on the pressure gradient.

3. Test cases

Our numerical model will be validated with two test cases related to overtopping of water waves, which are well known design problems in coastal and harbor engineering. The first one is over a smooth impermeable sea dike, and the second one over a vertical fixed barrier in the front of a pier. Both cases involve the surface waves breaking during overtopping, while static flows are disturbed by a wave generator, placed at the inlet, for the regular and irregular waves, respectively. Computations are performed in NWT, where a typical computational domain overlapping a dike includes a total length of 6.3 (m) and a height of 1 (m), as depicted in Fig. 13. The surface elevation at five wave gauges (herein abbreviated as WG0 to WG5) are measured for observation of the variation versus time, in which one of particular interest is on the dike crest, WG5 at $x = 5.9$ m (see Fig. 13). Three grid levels are separately implemented in order to study the grid refinement effects. A relatively fine grid with varying cell sizes, for example, is 251×40 in the x- and z-directions, respectively. Generally, each grid approximates one day or more than one week of the CPU time, dependent on a user-specified running time in the INPUT file. The calculated results are represented in terms of the wave-induced velocity fields in the x–z plane and time history of the surface elevation η (m) at a selected wave gauge. In this case, we define $x = 0$ and 6.3 (m) as the inlet and the outlet, respectively.

3.1. A sea dike

The geometry of the sea dike consists of the seaward slope (1:6), the landward one (1:3) and the dike crest h ($h = 0.8$ m) with the width s ($s = 0.3$ m), as illustrated in Fig. 13, where the corresponding dimensions are $l_1 = 1.0$ (m) and $l_3 = 0.5$ (m). With trivial effort, a nonuniform Cartesian cut-cell mesh that covers the dike is generated and fixed for entire computations (see Fig. 13 with one single block on a typical mesh: 205×40). An extra amount is to reconstruct the effectively computational domain by calculating the

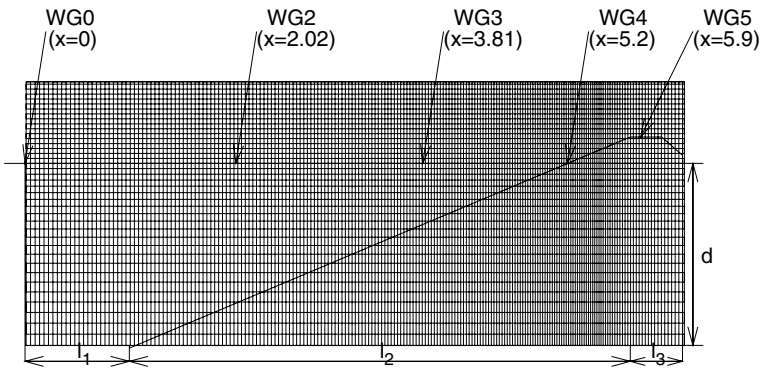

Fig. 13. Computational domain on a nonuniform Cartesian cut-cell mesh with grids (205×40) for sea dike problems. WG0 to WG5 represent five wave gauges (WG).

intersections of the geometric segments overlapping a Cartesian background grid, based on Newton's iteration algorithm, while curves (or surfaces in 3D) to describe the dike profile are approximated with a biquadratic function. This can be realized by predefining cells that are fully or partially dry, in which the former (called a whole obstacle or internal obstacle cell) is characterized as zero velocity and the latter is referred to as a cut cell (see Fig. 7). At the inlet, the characteristics of the regular wave (the wave height H, the wave period T and the finite water depth d in this case) are specified by the user (see Table 1).

3.2. Calculated results and discussions

3.2.1. Convergence history

Iterative convergence in this case is assessed by examining the L_2 norm of the residuals (Res) for the momentum equations (U, W) in the x- and z-directions, and the pressure (P) on the mesh. It is defined as

$$\mathrm{Res}_{\varphi} = \left\{ \sum_{m=1}^{N} (\varphi_{i,j,k}^{n} - \varphi_{i,j,k}^{n-1})^2 / N^2 \right\}^{1/2},$$

where the summation is carried out from $m = 1$ to N (the total number of cells) and φ represents (U, W, P).

Three curves for the residuals (U, W, P) are drawn on the two meshes, the coarse mesh (145×28) and the fine one (251×40), as illustrated in Fig. 14. This displays the convergence history of the point method (for the velocity) and the ICCG method (for the pressure) against time, respectively. As expected, the ICCG algorithm performs quite well due to its preconditioning technique. This achieves the fast convergence rates (see Fig. 14). Additionally, our computations show that it needs less computing time for a given level of convergence, as compared with the SOR scheme (where $\omega = 1.2$ for the overrelaxation parameter), when a Poisson equation for the pressure is resolved with these two approaches. On Cartesian cut-cell grids, therefore, the ICCG method can be considered as a more efficient iterative solver for updating the pressure. In our case, the pressure-velocity coupling is not enforced at each iteration. This is classified as a decoupled approach as opposed to a fully coupled algorithm. Generally, it is relatively straightforward in its implementation within a flexible framework [18,26], whereas the convergence behavior for the velocity in our test case is less satisfactory.

3.2.2. Grid refinement effects

The effects of increasing grid resolution on the wave-induced motions are studied with three grid levels, as illustrated in Fig. 15 for the velocity fields at a given time, and Figs. 16, 17 for the time history of the

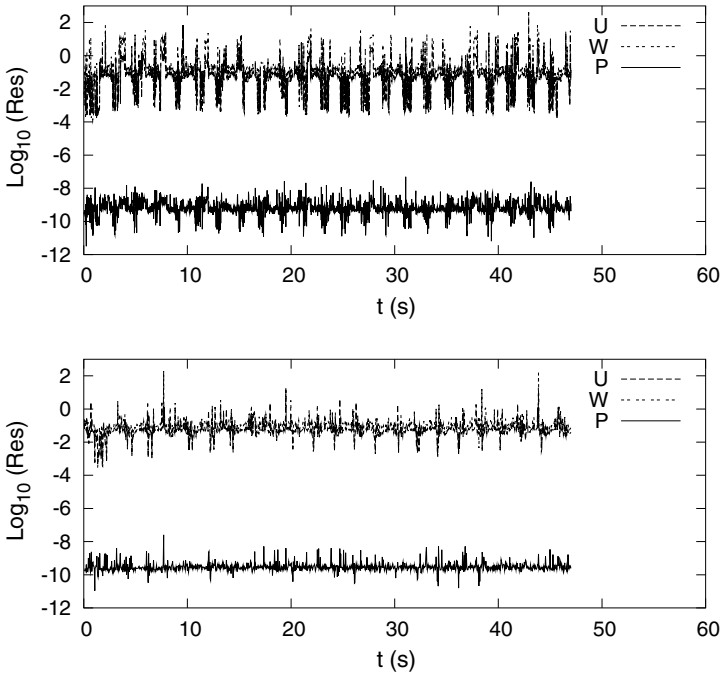

Fig. 14. Convergence histories of the L_2 norm of the residuals (U, W, P) on grids 145×28 (top) and 251×40 (bottom) for sea dike problems.

surface elevation at certain locations. By observation, it is found that differences attributed to the grid effects are relatively small for the surface elevation and mainly limited to the capture of fine structures for the velocity fields. A relatively fine mesh (251×40), therefore, may describe well the development of the regular waves. The discussion regarding this point is given as follows.

Generally, more detailed physical phenomena of motions can be represented with increased mesh refinement, as shown in Fig. 15, which provides an illustrative observation for the wave-induced velocity fields at $t = 4.4$ s. A common feature is that waves overtop at any mesh, naturally capturing the breaking waves in the surf zone. As expected, the shape of the front in this area tends to be more realistic as the mesh is refined but the localized velocity distributions vary rapidly with the present different grid size (see Fig. 15). Some reasons are interpreted as the fact that something with the coarsest mesh (145×28) is missing. For instance, it does not detect well motions due to insufficient grid resolution but the current two fine meshes $(205 \times 40,\ 291 \times 56)$ seem to help more or less. A local adaptive mesh [1,50,57] adjacent to interfaces is also attractive, especially on the crest of the dike, which will be studied in the next stage.

Interestingly, a regular shape of the wave profiles may be resolved adequately on all meshes, as shown in Figs. 16 and 17, especially for the latter that gives reliable evidence. Both demonstrate the influences of grids on the time trace of the surface elevation but the former is fixed at WG3 ($x = 3.81$ m) closer to region of the breaking waves. As can be observed, the wave trains on three meshes rapidly develop in the particular direction that the regular waves propagate at starting $t = 0$. Some discrepancies regarding the phase leg, however, are obvious under grid refinement (see Fig. 16). And it could be thought that the discrepancy of the results almost arises from the grid effects, since the reflection of waves from a structure is not significant or its appearance is little at shortly run time.

Next let's further compare with the experimental data available at WG2 ($x = 2.02$ m), as illustrated in Fig. 17 with 10 waves on three grid levels, where a grid on the finest mesh is 251×40 that we recommend.

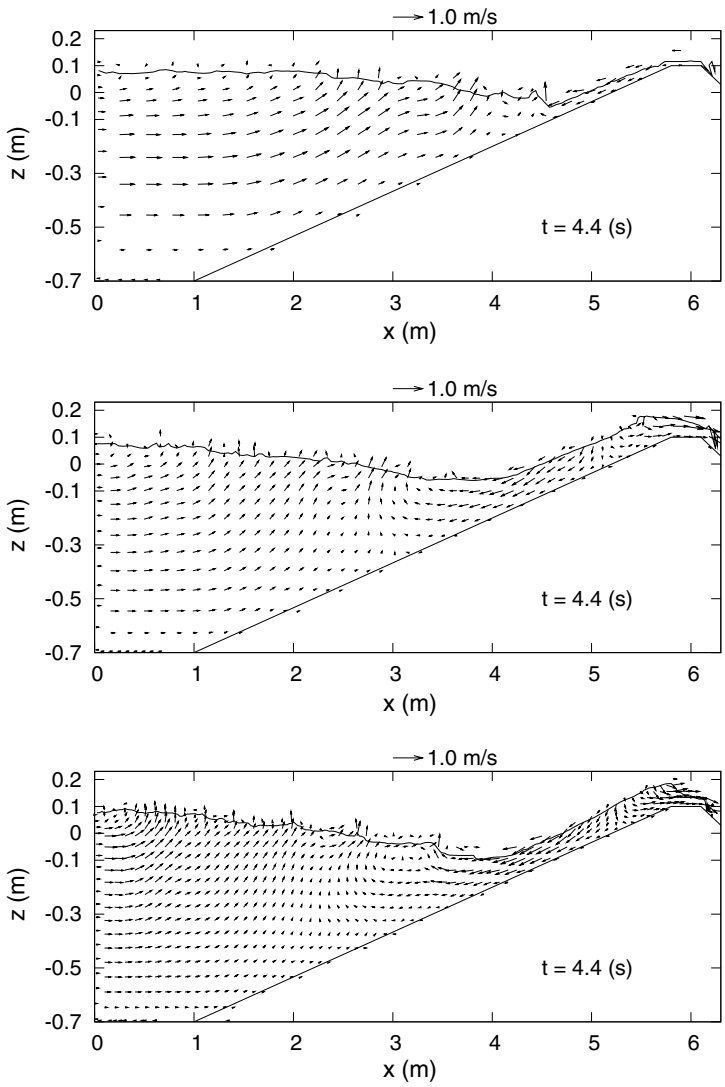

Fig. 15. Grid refinement effects for the wave-induced velocity fields at a given time $t = 4.4$ (s) with the coarsest mesh 145×28 (top), the fine 205×40 (middle) and the finest 291×56 (bottom).

First, the shape of waves between two successive cycles almost maintains the regularity, indicating that flows itself tend to be quasi-stationary. Second, all mesh can detect well the overall shape of the wave profiles that exhibits a feature of typical non-linearity: higher and narrower peak; and lower and flatter troughs, as shown in Fig. 17 (also see Figs. 16 and 18). Finally, the results agree well with the experimental data under mesh refinements, as shown in Fig. 17, which looks much more promising than Fig. 16: top, whereas there is a slight departure from the phase plus the overestimation for trough. Probably, the large difference between computations and measurements (see Fig. 16) may be attributed to the fact that the exact normal dynamics free-surface boundary condition (see Eq. (48)) should be considered, especially when flows become high turbulent. As a result, the current finest mesh may be suited to capture most of the wave-induced motions. A significant benefit is the CPU time required does not cost much more for Linux based PC.

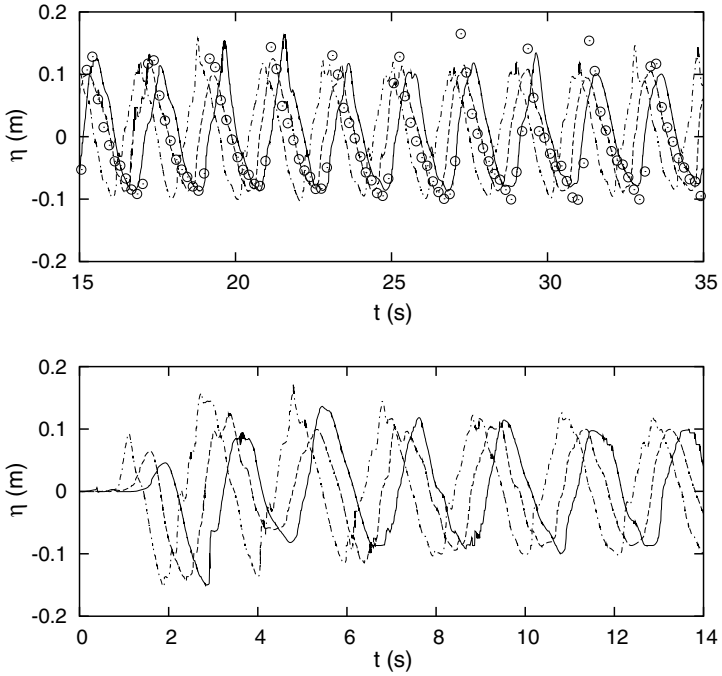

Fig. 16. Grid refinement effects for time history of the surface elevation at one wave gauge, WG3 ($x = 3.81$ m) for a sea dike. Top: a global observation (10 waves); bottom: a local view (7 initial waves). (—) 251×40; (– – –) 205×40; (– · –) 145×28; (⊙) measurement.

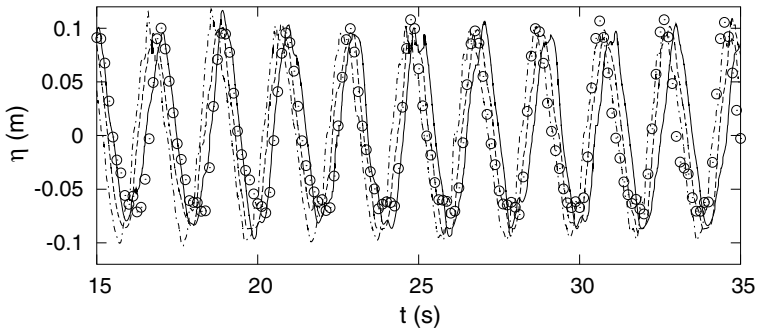

Fig. 17. Comparison of the calculated results with the experimental data for time history of the surface elevation at one wave gauge, WG2 ($x = 2.02$ m). (—) 251×40; (– – –) 205×40; (– · –) 145×28; (⊙) measurement.

Additionally, an intrinsic feature of our solver is that computations are stable during a long duration of simulation, indicating that the active damping terms (see Eq. (30)) do not cause excessive energy dissipation. In contrast, it may suppress the reflected waves like the sponge layer method [19].

3.2.3. Influences of turbulence models, surface tension and Reynolds number on the wave-induced motions

To further elucidate the mechanism and the dissipative features of physical processes involved, the following is to address the effects of the SGS models, surface tension and Reynolds number on the wave-induced motions, respectively, including the role of a turbulence model under waves breaking.

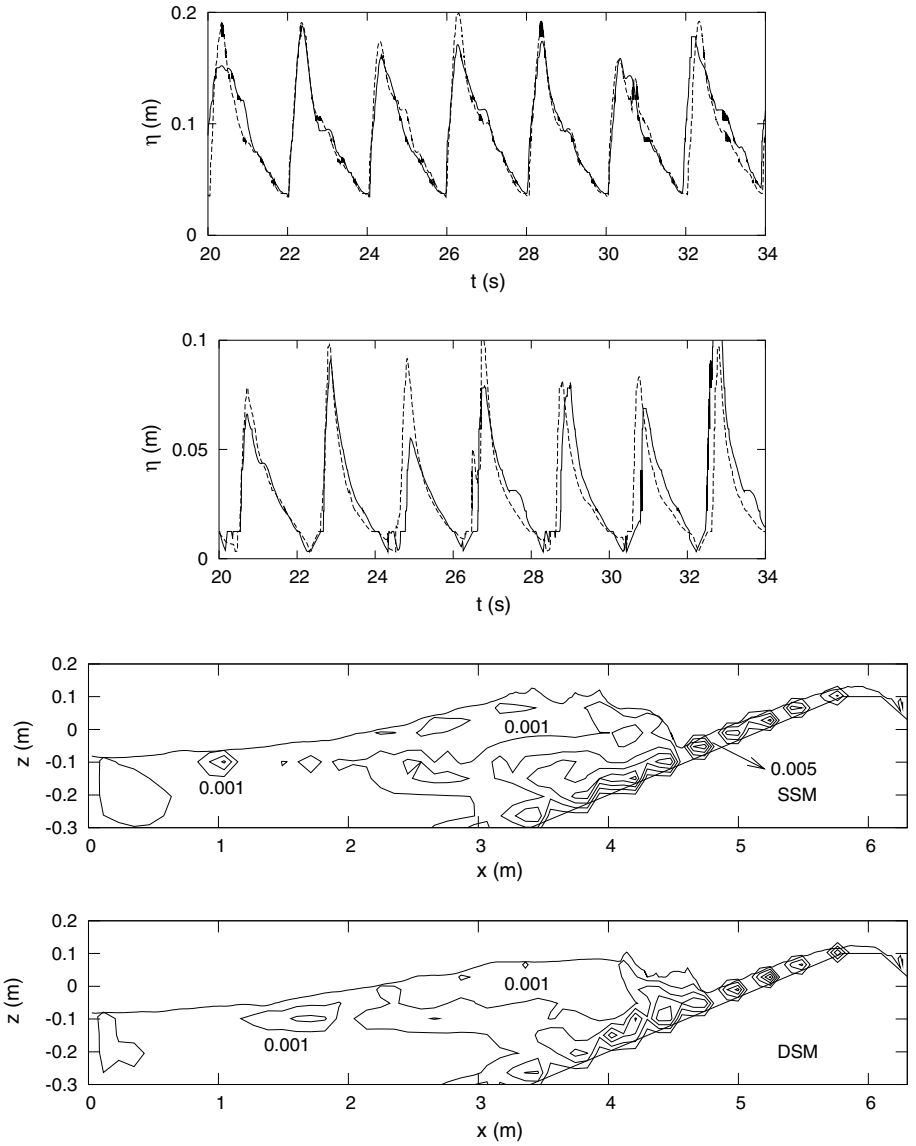

Fig. 18. SGS model effects on grids (251×40). From top to the next: WG4 ($x = 5.2$ m) and WG5 ($x = 5.9$ m) for time history of the surface elevation (SSM (—), DSM (– – –)). The last two: the eddy viscosity (ν_t) contours at $t = 7.5$ (s) (magnified view: 0.001 to 0.01 with interval 0.0015) using SSM and DSM, respectively.

3.2.3.1. The SGS models. Within the eddy-viscosity family, we select two Smagorinsky models for study of the influence of the SGS models on flows caused by the waves. One is the static Smagorinsky model, referred as to SSM. One is a dynamic Smagorinsky model [13] that adjusts itself the model constant in SSM (see Eq. (36)), called DSM. The results obtained with both models are given, as illustrated in Fig. 18 for the surface elevation against time at two wave gauges of interest: approximately at the surf zone (WG4, $x = 5.2$ m from the wavemaker, where flows display high turbulence), and on the dike crest (WG5, $x = 5.9$ m, where turbulent flows near walls are characterized by much less universal properties). Typically, these two gauges

directly record a signal from waves breaking and wave overtopping events, respectively. By comparison, the latter exhibits much more unevenly distributed in space and time (where, the surface elevation is measured with respect to the dike crest). In particular, it provides useful information for design of a dike like the layer thickness, the discharge and the cumulative overtopped volume of water.

Broadly, globally similar but distinctly different local features are apparent for these two models: SSM and DSM. Both reproduce the desirable shape that increases rapidly first and then diminishes slowly at each period, as shown in Fig. 18, which is similar as observed in the physical model. It is clear that DSM acts as less dissipative behavior near the wall than SSM with the van Driest damping. By comparison, a slight improvement is achieved with a dynamic LES, as illustrated in Fig. 19. Details of computations with DDM plus comparison with our monotonically integrated LES (MILES) approach, can be seen in our present work [29,30].

Theoretically, the free-surface boundary layer has to be taken into account, especially when waves break. Instead of $p = 0$ at the free surface (see Eq. (37)), the viscous normal dynamic free-surface boundary condition is given by [26]

$$p = \rho(v + v_t)\left\{2\frac{\partial w}{\partial z} - \frac{\partial h}{\partial x}\left(\frac{\partial u}{\partial z} + \frac{\partial w}{\partial x}\right) - \frac{\partial h}{\partial y}\left(\frac{\partial v}{\partial z} + \frac{\partial w}{\partial y}\right)\right\} \tag{48}$$

indicating that the effects of the SGS models on the free-surface can be captured via eddy viscosity v_t specified by Eq. (36), as illustrated in Fig. 18, where the shape of contours at $t = 7.5$ (s) displays the irregularity. As expected, the effects of the SGS models on the wave-induced flows are mainly confined to strongly turbulent regions, dependent on the distributions of the eddy viscosity. A high value of v_t more than 0.005, for example, is subjected to rapid deformation of the free-surface at about $x = 4.56$ (m). Consequently, this provides one possibility for study of the behavior of the LES model at the interface as done in our study [26,27], in which two turbulence models: Baldwin–Lomax's model and a $k - \varepsilon$ one, are applied for investigation of their effects on three-dimensional turbulent free-surface flows around modern ships with the help of a moving mesh. h in Eq. (48) represents the wave height, which can be achieved with the value of α, when using a VOF approach. In this case, the molecular viscosity $v = 1.4 \times 10^{-4}$ m^2/s.

3.2.3.2. Surface tension. Surface tension can capture the curvature-dependent interfacial effects, as illustrated in Fig. 20, which describes the evolution of the front shape at a certain time $t = 7.5$ (s) with and without surface tension, labelled (a) and (b), respectively. A magnified view is also included for microscopic observation. As usual, the surface tension coefficient is assumed as a constant by setting $\sigma = 72.8$ dynes/cm

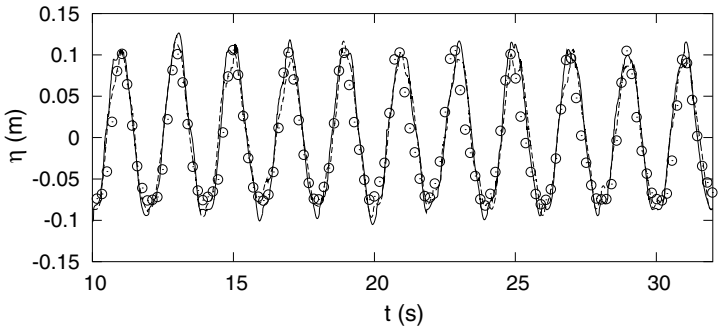

Fig. 19. Comparison of a dynamic LES with a static one for the surface elevation versus time at one point ($x = 2.02$ m). (—) a dynamic LES; (– – –) a static LES; (⊙) measurement.

in this case. In addition, we consider a case with high surface tension, that is, $\sigma = 145.6$ dynes/cm, two times coefficient larger than the original one, which is labelled (c).

Under surface tension, the effects on the solution are certain: this exhibits the strong hydrodynamic phenomena of breakup in the region of high turbulence. A feature is that the shape of the front in this area

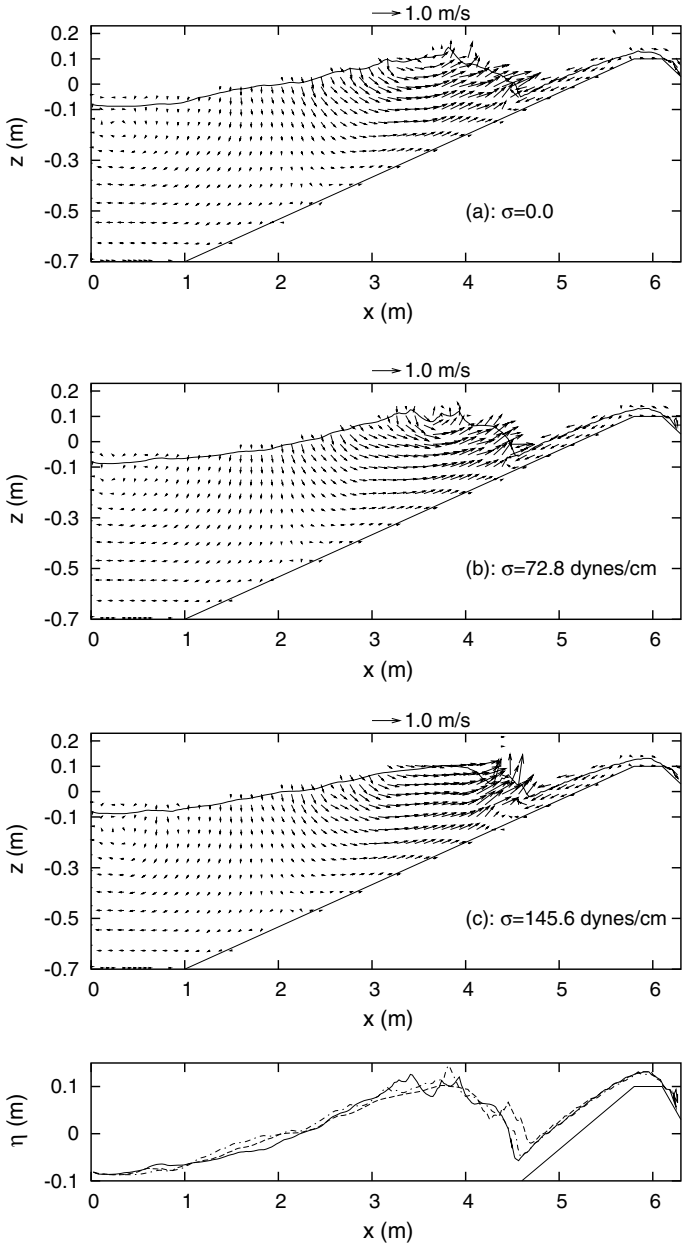

Fig. 20. The surface tension effects on grids (251×40) at $t = 7.5$ (s). (a) $\sigma = 0.0$; (b) $\sigma = 72.8$ dynes/cm; (c) $\sigma = 145.6$ dynes/cm for the wave-induced velocity fields. Bottom for distributions of the surface elevation in space: $(-\cdot-)\sigma = 0.0$, (—) $\sigma = 72.8$, $(--)\sigma = 145.6$ (magnified view).

is changed drastically, and the strong vortex exists (see Fig. 20). In the presence of higher surface tension ($\sigma = 145.6$ dynes/cm), the shape of the front tends to break significantly. Hence, the substantial difference in small scale structures is obvious when surface tension is present or not, whereas its effect is minor in the most ranges, dependent on the deformation of the free-surface.

3.2.3.3. Reynolds number. On the assumption that Reynolds number (R_n) that describes a flow characteristic is defined as $R_n = \frac{g^{\frac{1}{2}} d^{\frac{3}{2}}}{\nu}$ (where, d is the constant finite water depth), thus the effects of R_n on flows can be realized through the increase of $R_n = 1.4 \times 10^4$ to 1.8×10^6, as shown in Fig. 21. No much difference, for example, is observed for the time history of the surface elevation at WG5, indicating that the effect due to the change of R_n is weak for the capture of the surface elevation, although complex shear flows caused by the waves are dominated on the dike crest. A similar conclusion can be drawn as in the case of WG4. It is clear that the current grid resolution (251×40) cannot fully describe the boundary layer. Meshes close to the wall need sufficient refinement, which allows a more accurate prediction for the thin boundary layer, as R_n increases. In this work, we focus attention on the capture of highly non-linear waves, propagating from the deep water to the shallow one, although a wall friction that acts as the energy dissipation will alter the formation of the layer thickness in this area. In particular, LES simulation of wall-bounded flows is prohibitively expensive. Dynamics of the flow in the wall proximity, therefore, are likely to be affected by inadequately meshing in the near-wall region, once the slip conditions are used on the wall. One approach to avoid this problem is that LES may be combined with a wall-layer model [45,58], where it may be conducted on a relatively coarse grid.

3.2.3.4. The role of a turbulence model in the case of breaking waves. Flows become highly turbulent when waves continuously break in the surf zone. In such a case, the energy of waves accumulated needs to be dissipated, for example, by turbulence. Since eddies gradually spread, otherwise, spurious currents are generated in the flowfield, as illustrated in Fig. 22 at two larger time levels: $t = 12.9$ and 30.3 s for one test case, which is defined as no viscosity due to $\nu_{\text{eff}} = 0$ to be enforced. But with the introduction of a SGS

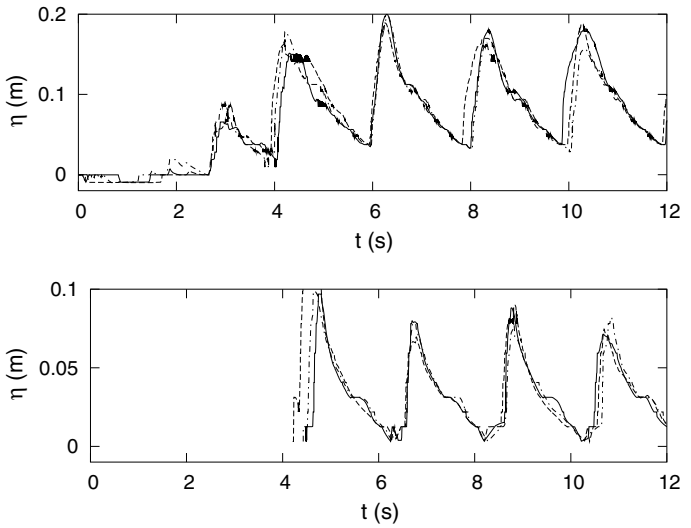

Fig. 21. The Reynolds number effects at WG4 (top) and WG5 (bottom) for the surface elevation versus time on grids (251×40). (—) $R_n = 1.8 \times 10^6$; (– – –) 1.8×10^5; (– · –) 1.4×10^4.

model, it is found that the unphysical currents at the corresponding time transient, which develop a kind of turbulence, are disappeared. In this way, flows tend to more realistic in the corresponding area. In particular, the calculated results with a LES look much better than those with no viscosity as compared with measurements available for sea dike problems. Consequently, it is clear that adequate turbulence model is required for problems related to simulation of the breakwater, indicating that computations based on

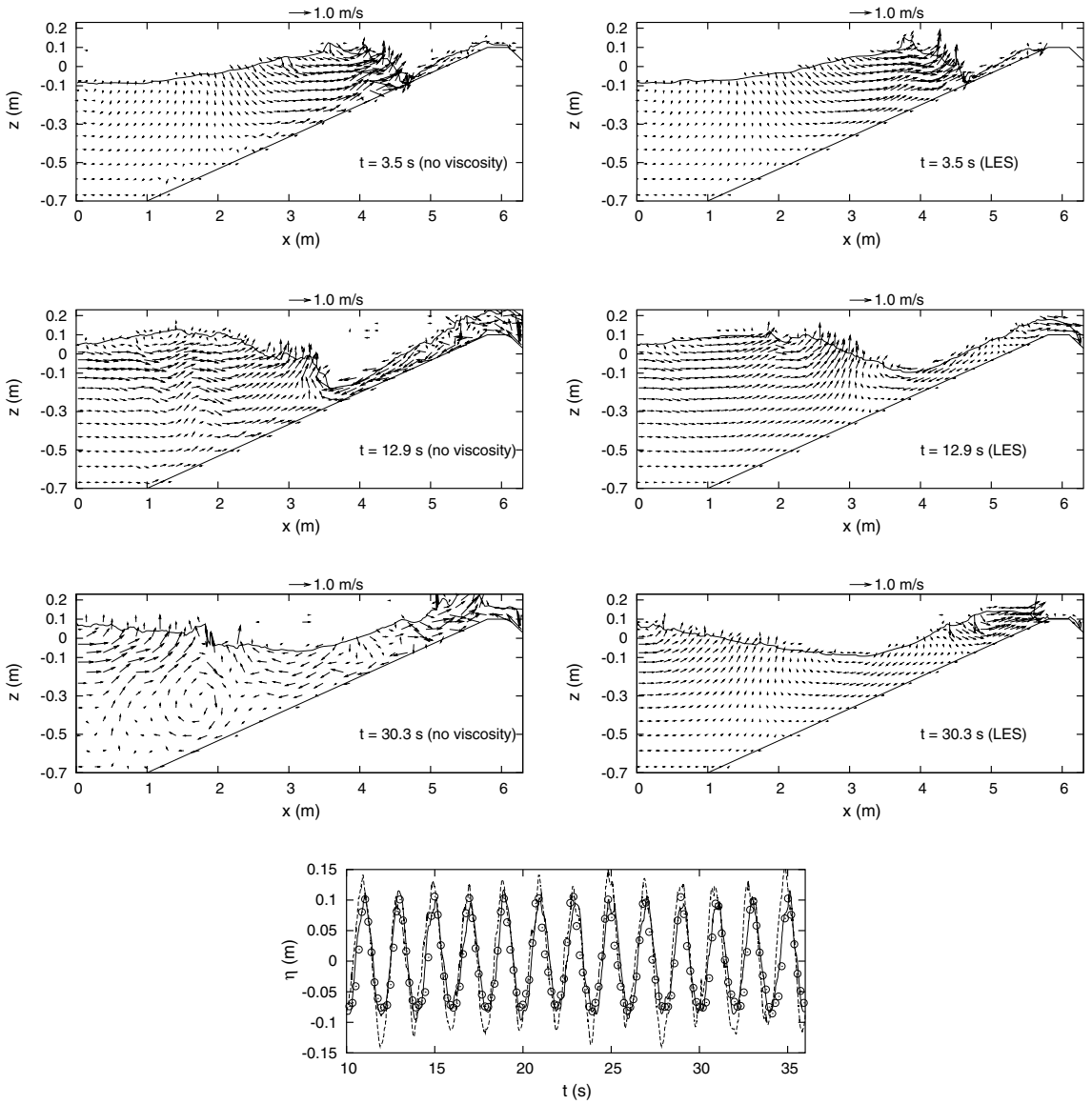

Fig. 22. The effects of a LES model on the wave-induced velocity fields at given time levels. Left: no viscosity; right: a static LES. Bottom: comparison of the surface elevation versus time at a certain point ($x = 2.02$ m) for sea dike problems. (—) LES; (– – –) no viscosity; (⊙) measurement.

inviscid flows are not sufficient for accurate description. This is due to the fact that the potential flow approach without any viscous terms cannot capture energy dissipation by viscous effects under breaking waves. But it exists in a physical model, and it may be interpreted as turbulence induced by breaking waves. As expected, a turbulence model-based solver can give a better accuracy than the potential flow solution. Note that the current case is done for a 2D large-eddy simulation (LES) model. A 3D test case could be better since simulations may depend on the small-scale 3D flows [10]. Additionally, at this stage we do not account for the effects of trapped air pockets during and after wave breaking, since the conventional assumption regarding continuous and material surface on a free surface is no longer valid [32]. In case the air is entrained in the water, whether in the form of small bubbles or a larger air pocket, compressibility effects become important. The surface capturing approaches [21], therefore, can describe this one naturally. Moreover, the overtopping zone may be modelled realistically once the wall adhesion effects are involved. Further study, therefore, is necessary to clarify these issues.

3.2.4. An observation of the wave-induced velocity fields with several stages

With the help of an animation available, one can observe the wave-induced motions in the region of interest with several stages: the wave attack, the runup, the rundown, the waves breaking to overtopping of waves. In this paper, just some selected results are provided, as illustrated in Figs. 23–25 for a visualisation of the velocity fields at a series of given time.

3.2.4.1. Over a sea dike. As more waves pass through the dike crest, the flow becomes fully turbulent and sustained after an initial transient period so that the features of the flow pattern tend to be very complex, often subjected to the steepness of the free surface most likely associated with a cycle of splashing and the

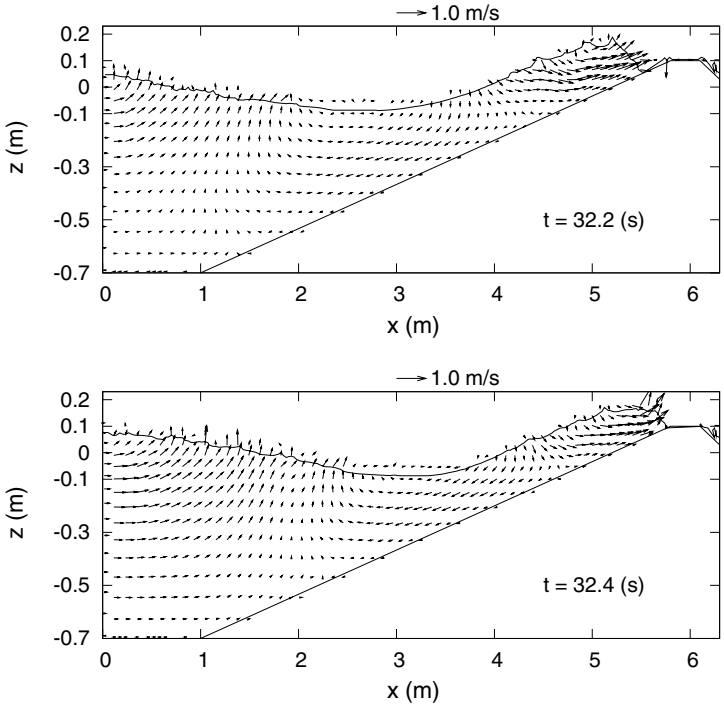

Fig. 23. Velocity fields caused by the regular waves over a sea dike from $t = 32.2$ to 32.4 (s) on grids (251×40).

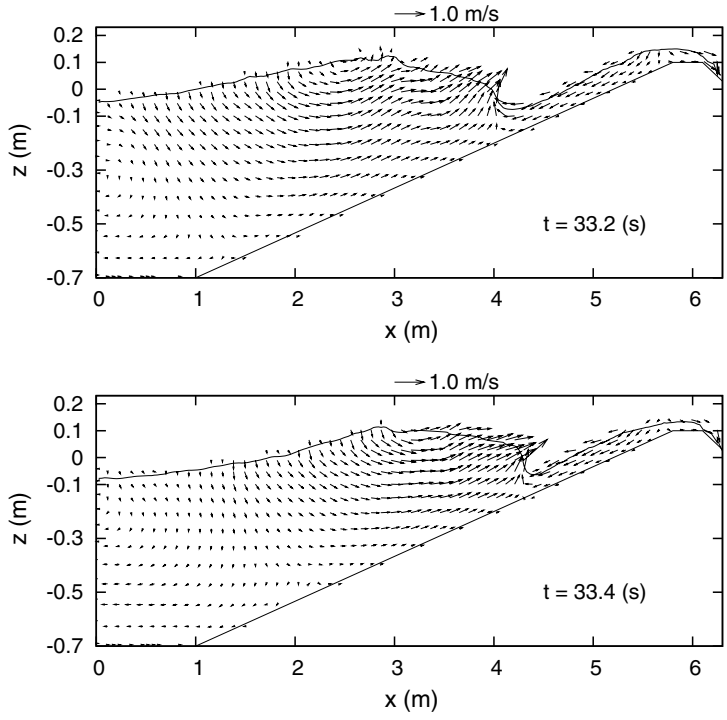

Fig. 24. Velocity fields caused by the regular waves over a sea dike from $t = 33.2$ to 33.4 (s) on grids (251×40).

vortex formation created by the velocity. Waves continuously break, while the energy of waves is dissipated by turbulence and convected by vortices.

Now we describe the corresponding motions in Figs. 23 and 24. At $t = 32.2$ (s), the wave height increases as it shoals on the front face. A violent overtopping jet will occur again at $t = 32.4$ s. When it propagates towards the dike crest, the front of waves declines gradually downstream. Consequently, its further steepening causes the initiation of wave breaking process and then the rapid decrease of the surface elevation. By 33.2 (s), some particles still move upwards but the major portion of flows on the slope displays the proceeding of the downwash under the gravitational acceleration, while the next wave is approaching the dike. This leads to a strong backflow and the waves break on the upper reach of the dike at $t = 33.4$ (s), indicating that the free surface is significantly deformed at the intersection (about $x = 4.2$ m) of the incoming waves with the backflow. In the wave front, the particle velocity exceeds the speed limit underneath the region of flows, forming a layer often referred to as the roll and creating a large hydraulic jump nearby, which can be considered as a shock wave. Our solver, therefore, captures the major features of flows: overtopping of surface waves breaking. In particular, the velocity and the pressure interact strongly each other when the interface undergoes severe topological changes.

3.2.4.2. Over a vertical fixed barrier in front of pier. Finally, we study another case: violent wave overtopping over a vertical fixed barrier, which shelters coastal structures from the direct impact of steep waves. This is of particular interest for validation of our VOF-based solver, where surface waves naturally break against the structure, throwing the water over its top. Results obtained with irregular waves are illustrated in Fig. 25 for the time history of the surface elevation at one point ($x = 3.81$ m) close to the barrier and the corresponding velocity fields at certain time, where the irregular waves are created by superimposing a

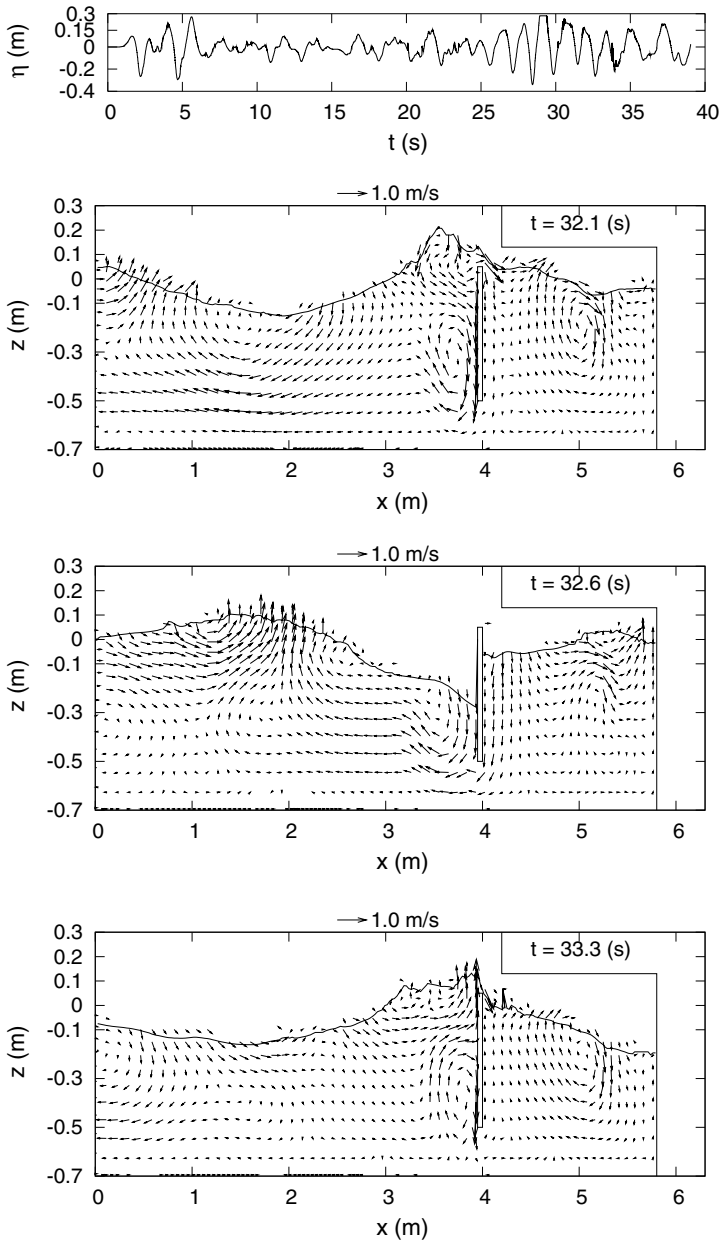

Fig. 25. Time history of the surface elevation at one point ($x = 3.81$ m) and velocity fields caused by the irregular waves over a vertical fixed barrier from $t = 32.1$ to 33.3 (s) on grids (251×40).

series of regular waves. It is clear that motions caused by the irregular waves look much more complex than those by the regular waves. As expected, a vortex generated in the vicinity of the barrier characterizes the dynamics of the wave-induced turbulent motions at the smallest scale in this case. More details of computations regarding this one can be seen in our current work using the same solver based on a dynamic LES [29].

4. Conclusions

We developed a novel solver for the simulation of wave overtopping over sloping and vertical structures in a NWT. Its major advantage is that a simple VOF approach is designed for effective modelling of a very sharp interface. This has been applied in combination with an unsteady incompressible Navier–Stokes solver that includes the TVD-type schemes for sharp gradients capturing and fully implicit cell-staggered FV approaches on nonuniform Cartesian cut-cell meshes. Two essential features in our solver are the ability to describe overtopping of breaking waves and a computationally efficient algorithm for the coupling of the pressure with the velocity based on a projected method. The results obtained in complex topology flows induced by regular and irregular waves are very encouraging, especially since they compared well with the experimental data available. Overall, our solver is able to yield detailed information for wave-structure interaction problems. The main conclusions are drawn as follows:

- The grid dependency may be an aspect that is crucial for the VOF solver problems. In our study, it is found that differences attributed to gridding are weak for the capture of the surface elevation but the essential details of the resolution can be captured as the mesh is refined, especially for the accurate description of the wave-induced velocity fields.
- Without excessive energy dissipation, the introduction of a blend of the second- and fourth-order artificial damping terms helps to eliminate spurious oscillations during lengthy computations, as the corresponding coefficients that control the artificial dissipation are given adaptively.
- With an absorbing-generating boundary condition, an additional feature is that the solution is able to specify a well-suited boundary value for α, which helps to resolve the volume fractions in VOF.
- Handling implicitly the pressure over mixed cells and modelling of surface tension as a body force simplify significantly the treatment of the normal dynamics free-surface boundary condition, especially when interfaces undergo severe topological change. It is found that the simulation of breaking waves looks more realistic under the surface tension effects.
- With implicit interface reconstruction, the solution of the transport equation for the volume fractions is simple but effective according to the currently proposed approach.
- For problems associated with the simulation of breaking waves, it is found that the introduction of an adequate turbulence model may be necessary.

  Ongoing and future work will incorporate a test case on $3D$.

Acknowledgements

The present work is carried out within the research project G.0228.02 funded by the Funds for Scientific Research – Flanders (Belgium), and the EU-project CLASH (EVK3-CT-2001-58). We would like to thank Dr. Schüttrumpf in Leichtweiss-Institut für Wasserbau, Braunschweig, Germany, who provided the experimental data for this dike. Additionally, we also thank the referees for their helpful suggestions.

References

[1] A.S. Almgren, B.B. Joun, P. Colella, L.H. Howell, M. Welcome, A conservative adaptive projection method for the variable density incompressible Navier–Stokes equations, J. Comp. Phys 142 (1998) 1–46.

[2] E. Aulisa, S. Manservisi, R. Scardovelli, S. Zaleski, A geometrical area-preserving volume-of-fluid advection method, J. Comp. Phys. 192 (2003) 355–364.

[3] J.P. Boris, D.L. Book, Flux-corrected transport I. SHASTA, a fluid transport algorithm that works, J. Comp. Phys. 11 (1973) 38–69.

[4] J.U. Brackbill, D.B. Kothe, C. Zemach, A continuum method for modelling surface tension, J. Comp. Phys. 100 (2) (1992) 335–354.

[5] R.K.C. Chen, R.L. Street, A computer study of finite amplitude water waves, J. Comp. Phys. 6 (1970) 68–94.
[6] E.D. Christensen, R. Deigaard, Large eddy simulation of breaking waves, Coast. Eng. 42 (2001) 53–86.
[7] A.J. Chorin, A numerical solution for solving incompressible viscous flow problems, J. Comp. Phys. 2 (1967) 12–26.
[8] P. Colella, P.R. Woodwrad, The piecewise parabolic method (PPM) for gas dynamic simulations, J. Comp. Phys. 54 (1984) 174.
[9] J.H. Ferziger, M. Peric, Computational Methods for Fluid Dynamics, second ed., Springer, Berlin, 1999.
[10] C. Fureby, Larger-eddy simulation of turbulent anisochoric flows, AIAA J. 33 (1995) 1263–1272.
[11] E. Garnier, M. Mossi, P. Sagaut, P. Comte, M. Deville, On the use of shock-capturing schemes for large-eddy simulation, J. Comp. Phys. 153 (1999) 273–311.
[12] L. Gentaz, C. Maury, B. Alessandrini, G. Delhommear, Numerical simulation of a two-dimensional wave tank in viscous fluid, Int. J. Offshore Polar Eng. 10 (2000) 1–9.
[13] M. Germano, U. Piomelli, P. Moin, W. Cabot, A dynamic subgrid-scale eddy viscosity model, Summer Program, Center for Turbulence Research, Stanford University, Stanford, CA, 1990.
[14] D. Gueyffier, J. Li, A. Nadim, R. Scardovelli, S. Zaleski, Volume-of-fluid interface tracking with smoothed surfaces stress methods for three-dimensional flows, J. Comp. Phys. 152 (1999) 423–456.
[15] D.J.E. Harvie, D.F. Fletcher, A new volume of fluid algorithm: the defined donating region scheme, Int. J. Numer. Meth. Fluids 35 (2001) 151–172.
[16] C.H. Hirsch, in: Numerical Computation of Internal and External Flows, vol. 2, Wiley, New York, 1989.
[17] C.W. Hirt, B.D. Nichols, Volume of fluid method for the dynamics of free boundaries, J. Comp. Phys. 39 (1981) 201–225.
[18] B.R. Hodges, R.L. Street, On simulation of turbulent nonlinear free-surface flows, J. Comp. Phys. 151 (1999) 425–457.
[19] M. Israeli, S.A. Orszag, Approximation of radiation boundary conditions, J. Comp. Phys. 41 (1981) 115–131.
[20] A. Jameson, W. Schmidt, E. Turkel, Numerical simulation of the Euler equations by finite volume methods using Runge–Kutta time stepping schemes, AIAA 5th CFD Conf., AIAA Paper 81-1259, 1981.
[21] F.J. Kelecy, R.H. Pletcher, The development of a free surface capturing approach for multidimensional free surface flows in closed containers, J. Comp. Phys. 138 (1997) 939–980.
[22] D.S. Kershaw, The incomplete Cholesky-conjugate gradient method for the iterative solution of system of linear equation, J. Comp. Phys. 26 (1) (1978) 43–65.
[23] N. Kobayashi, A.K. Otta, I. Roy, Wave reflection and runnup on rough slopes, J. Waterway Port Coast. Ocean Eng., ASCE 113 (3) (1987) 282–298.
[24] B. Lafaurie, C. Nardone, R. Scardovelli, S. Zaleski, G. Zanetti, Modelling merging and fragmentation in multiphase flows with SURFER, J. Comp. Phys. 113 (1994) 134–147.
[25] T. Li, J. Matusiak, R. Lehtimåki, Numerical simulation of viscous flows with free surface around realistic hull forms with transom, Int. J. Numer. Meth. Fluids 37 (2001) 601–624.
[26] T. Li, Computation of turbulent free-surface flows around modern ships, Int. J. Numer. Meth. Fluids 43 (2003) 407–430.
[27] T. Li, Effects of grid refinements and turbulence models on ship-induced waves, Int. Shipbuild. Proger. 50 (3) (2003) 255–272.
[28] T. Li, P. Troch, J. De Rouck, A solver for numerical simulation of breaking waves using a cut-cell VOF cell-staggered finite-volume approach, Report, Department of Civil Engineering, Ghent University, Belgium, 2003.
[29] T. Li, P. Troch, J. De Rouck, A dynamic LES of breaking waves during overtopping, in preparation.
[30] T. Li, P. Troch, J. De Rouck, Large eddy simulation of wave overtopping on nonuniform cartesian cut-cell grids, in: Proceedings of the 14th International Offshore and Polar Engineering Conference, Toulon, France, May 23–28, 2004.
[31] P. Lin, P.L.F. Liu, Internal wave-maker for Navier–Stokes equations models, J. Waterway Port Coast Ocean Eng. 4 (1999) 207–215.
[32] P. Lin, P.L.F. Liu, A numerical study of breaking waves in the surf zone, J. Fluid Mech. 359 (1998) 239–264.
[33] B. Meric, J. Steellant, J. Vierendeels, K. Riemslagh, E. Dick, Computational treatment of source terms in two-equation turbulence model, AIAA J. 38 (11) (2000) 2085–2093.
[34] H. Miyate, M. Zhu, O. Watanabe, Numerical study on a viscous flow with free-surface waves about a ship in steady course by a finite-volume method, J. Ship Res. 36 (1992) 332–345.
[35] J.J. Monaghan, Simulating free surface flows with SPH, J. Comp. Phys 110 (1994) 399–406.
[36] I. Orlanski, A simple boundary condition for unbounded hyperbolic flows, J. Comp. Phys. 21 (1976) 251–269.
[37] S. Osher, J.A. Sethian, Fronts Propagating with curvature-development speed: algorithm based on Hamilton–Jacobi formulations, J. Comp. Phys. 79 (1998) 12–49.
[38] J.C. Park, M.H. Kim, H. Miyata, Full non-linear free-surface simulations by a 3D viscous numerical wave tank, Int. J. Numer. Meth. Fluids 29: (1999) 685–703.
[39] H.A.H. Petit, P. Tonjes, M.R.A. van Gent, P. van den Bosch, Numerical simulation and validation of plunging breaking using a 2D Navier–Stokes model, in: Proc. 24th Int. Conf. Coast. Energy, ASCE, Reston, VA, 1994, pp. 511–534.

[40] E.G. Pucket, A.S. Almgren, J.B. Bell, D.L. Marcus, W.J. Ride, A high-order projection method for tracking fluid interface in variable density incompressible flows, J. Comp. Phys. 130 (1997) 269–282.
[41] C.M. Rhie, W.L. Chow, Numerical study of the turbulent flow past an airfoil with trailing edges separation, AIAA J. 21 (11) (1983) 1525–1532.
[42] W.J. Rider, D.B. Kothe, Reconstructing volume tracking, J. Comp. Phys. 141 (1998) 112–152.
[43] P.L. Roe, Approximate Riemann solvers, parameter vectors and difference schemes, J. Comp. Phys. 43 (1981) 337–372.
[44] S.E. Rogers, Comparison of implicit schemes for the incompressible Navier–Stokes equations, AIAA J. 33 (1995) 2066–2072.
[45] R.C. Schmidt, A.R. Kerstein, S. Wunsch, V. Nilsen, Near-wall LES closure based on one-dimensional turbulence modelling, J. Comp. Phys. 186 (2003) 317–355.
[46] M. Rudman, Volume-tracking methods for interfacial flow calculations, Int. J. Numer. Meth. Fluids 24 (1997) 671–691.
[47] R. Scardovelli, S. Zaleski, Interface reconstruction with least-square fit and split Eulerian–Lagrangian advection, Int. J. Numer. Meth. Fluids 41 (2003) 251–274.
[48] J. Smagorinsky, General circulation experiments with the primitive equations, part I: the basic experiment, Mon. Weather Rev. 91 (1962) 99–152.
[49] M. Sussman, P. Smereka, S. Osher, A level set approach for computing solutions to incompressible two-phase flow, J. Comp. Phys. 114 (1994) 146–159.
[50] M. Sussman, A.S. Almgren, J.B. Bell, P. Colella, L.H. Howell, M.L. Welcome, An adaptively level set approach for incompressible two-phase flows, J. Comp. Phys. 148 (1999) 81–124.
[51] M. Sussman, E.G. Puckett, A coupled level set and volume-of-fluid method for computing 3D and axisymmetric incompressible two-phase flows, J. Comp. Phys. 162 (2000) 301–337.
[52] P. Troch, J. De Rouck, An active wave generated-absorbing boundary condition for VOF type numerical model, Coast. Eng. 38 (1999) 223–247.
[53] O. Ubbink, R.I. Issa, A method for capturing sharp fluid interfaces on arbitrary meshes, J. Comp. Phys. 153 (1999) 26–50.
[54] H.S. Udaykumar, R. Mittal, W. Shyy, Computation of solid–liquid phase fronts in the sharp interface limit on fixed grids, J. Comp. Phys. 153 (1999) 535–574.
[55] S.O. Unverdi, G. Tryggvason, A front-tracking method for viscous, incompressible multifluid flow, J. Comp. Phys. 100 (1992) 25–37.
[56] B.L. Van, Towards the ultimate conservative difference scheme IV. A new approach to numerical convection, J. Comp. Phys. 23 (1977) 276–299.
[57] S. Vincent, J.P. Caltagirone, A one-cell local multigrid method for solving unsteady incompressible multiphase flows, J. Comp. Phys. 163 (2000) 172–215.
[58] M. Wang, P. Moin, Dynamic wall modeling for large-eddy simulation of complex turbulent flows, Phys. Fluids 7 (14) (2002) 2043–2051.
[59] Y. Watanabe, H. Saeki, Three-dimensional large eddy simulation of breaking waves, Coast. Eng. J. 41 (1999) 281–301.
[60] F. Xiao, A computational model for suspended large rigid bodies in 3D unsteady viscous flows, J. Comp. Phys. 155 (1999) 348–379.
[61] D.L. Youngs, Time-dependent multi-material flow with large fluid distortion, in: K.W. Morton, M.J. Baines, (Eds.), Numerical Methods for Fluid Dynamics, 1982.
[62] S.T. Zalesaki, Fully multi-dimensional flux corrected transport algorithm for fluid flow, J. Comp. Phys. 31 (1979) 335–362.